Modeling Alcogel Aging for Cycle Time Reduction and Measurement of Related Thermophysical Properties

A thesis

submitted by

David B. Orellano

In partial fulfillment of the requirements for the degree of

Master of Science

in

Mechanical Engineering

TUFTS UNIVERSITY

May 2011

ADVISER:

Professor Vincent P. Manno

ABSTRACT

Modeling Alcogel Aging for Cycle Time Reduction and Measurement of Related Thermophysical Properties

by

David B. Orellano

The thermal aging of silica alcogels in an alcohol solution is an important step in the production of fiber reinforced aerogel insulation. However, aging is time consuming and process limitations at the manufacturing scale are not well understood. Two approaches have been taken to develop a better understanding of aging with the goal of process acceleration. First, the thermal conductivity of fiber reinforced silica alcogel has been measured as a function of aging time using the transient line-source technique and property change has been considered as a means of process monitoring. Alcogel thermal conductivity was found to be 0.23-0.28 W/m·K, decreasing by 5-8 % after 6 hours of aging at 60 °C. The wide range in measured values has been attributed to variations in reinforcing fiber density. Second, representative models of fluid flow and heat transfer during a manufacturing scale aging process were created and process limitations were explored. Designing the aging process to allow for alcohol flow was found to have the ability to decrease aging times by as much as 3 hours.

Acknowledgements

I would first like to thank the members of my committee. Vincent Manno, thank you for all of your guidance and support these past two years. You have been a wonderful advisor. Douglas Matson, thanks for all of your help planning the experiments of this thesis and interpreting their results. Sara Jaworowicz, thank you for coming back to Tufts and supporting a fellow Jumbo.

Thank you to the professors and researchers on the Tufts aerogel team: Marc Hodes, Luisa Chiesa, Rich Wlezien, Peter Wong, Sarah Briggs, Justin Griffin, Drew Mills, Matt Sherman, and Jason Prapas.

Mez Polad and George Gould, thank you both for your technical support. Your willingness to share information and resources and to discuss aerogel manufacturing with me at length has been greatly appreciated.

Dyanne Della Pasqua, Lorin Polidora, Jim Hoffman and Vinnie Miraglia, many thanks for all of your technical and logistical support.

Finally, I would like to thank Aspen Aerogels and acknowledge the support of the Department of Energy under Award Number DE-EE0000266.

Disclaimer

This report was prepared as an account of work sponsored by an agency of the United States Government. Neither the United States Government nor any agency thereof, nor any of their employees, makes any warranty, express or implied, or assumes any legal liability or responsibility for the accuracy, completeness, or usefulness of any information, apparatus, product, or process disclosed, or represents that its use would not infringe privately owned rights. Reference herein to any specific commercial product, process, or service by trade name, trademark, manufacturer, or otherwise does not necessarily constitute or imply its endorsement, recommendation, or favoring by the United States Government or any agency thereof. The views and opinions of authors expressed herein do not necessarily state or reflect those of the United States Government or any agency thereof.

TABLE OF CONTENTS

ABSTRACT ii

ACKNOWLEDGEMENTS iii

DISCLAIMER iv

LIST OF FIGURES vii

LIST OF TABLES ix

NOMENCLATURE xiii

CHAPTER

I. Introduction 1

II. Background 5

2.1 Aerogel Synthesis 5
2.1.1 Gelation 5
2.1.2 Aging 7
2.1.3 Drying 12
2.2 Measuring Thermal Conductivity 13
2.2.1 The Transient Line-Source Technique 13
2.2.2 Derivation 15

III. Experimental Methodology and Measurements 20

3.1 Methodology 20
3.1.1 Probe Construction and Calibration 21
3.1.2 Sample Preparation 22
3.1.3 Testing 24
3.1.4 Experimental Uncertainty 26
3.2 Results and Discussion 26

IV. Modeling 32

4.1 Aging Vessel Data and Observations 32
4.2 Spacer Gap Model 35
4.2.1 Geometry and Material Properties 35
4.2.2 Governing Equations 37
4.2.3 Results 39
4.2.4 Mesh Independence Studies 41
4.3 Conduction Model 44
4.3.1 Geometry and Material Properties 45
4.3.2 Governing Equations 45
4.3.3 Results 47
4.4 Discussion 48

V. Conclusions and Future Work 50

BIBLIOGRAPHY 51

LIST OF FIGURES

Figure

1.1 Aspen Aerogels' manufacturing cycle 2

2.1 Polymerization and coarsening of an alcogel [1] 7

2.2 Linear drying shrinkage and bulk density of a subcritically dried gel as a function of aging temperature [2] 10

2.3 Average pore size of a subcritically dried gel as a function of aging temperature [2] 10

2.4 Pore size distribution of TEOS-based alcogel [3] 11

2.5 Line-source heater temperature response 15

3.1 Line-source probe for measuring thermal conductivity 21

3.2 Fiber reinforced alcogel sample with line-source probe 23

3.3 Circulating water heated aging bath 24

3.4 Experimental setup 25

3.5 Preliminary thermal conductivity results 27

3.6 Thermal conductivity separated by date of sample gelation 29

3.7 Thermal conductivity results using new H5 30

4.1 Temperature at various locations in Blanket 1 33

4.2 Temperature at various locations in Blanket 2 34

4.3 Representative geometry of the Spacer Gap Model 36

4.4 Velocity profile in the spacer gap subdomain. 40

4.5 Average gel roll temperature. 40

4.6 Temperature of the center of the spacer gap at various times. 41

4.7 Spacer Gap Model results compared to aging vessel temperature data . . . 42

4.8 Representative geometry of the Conduction Model 45

4.9 Conduction Model results compared to aging vessel temperature data . . . 47

4.10 Summary of modeling results and aging vessel data 49

LIST OF TABLES

Table

3.1 Alcogel and Aging Solution Recipes 23

3.2 Uncertainties associated with the thermal conductivity experiment 26

3.3 Summary of preliminary thermal conductivity results 27

3.4 Summary of thermal conductivity results using new H5 30

4.1 Spacer Gap Model material properties [4], [5] 37

4.2 Spacer Gap Model flow boundary conditions 38

4.3 Spacer Gap Model heat transfer boundary conditions 39

4.4 Mesh independence study results for the Spacer Gap Model 44

4.5 Conduction Model material properties [4] 45

4.6 Conduction Model boundary conditions 46

Nomenclature

Variables

α	Thermal diffusivity
β	Solid-liquid contact angle
γ	Euler's constant
γ_{LV}	Liquid-vapor surface tension
δ	Minimum dimension
θ	Dimensionless temperature
κ	Permeability
λ	Eigenvalue
μ	Dynamic viscosity
ρ	Density
ϕ	Porosity
ψ	Critical simulation variable
A	Element area
c	Specific heat capacity
d	Diameter
e	Relative error
h	Representative cell size
F	Body force
h	Representative cell size
$\bar{h}$	Average heat transfer coefficient

H	Height
I	Current
$\mathbf{I}$	Identity matrix
J	Fluid flux
k	Thermal conductivity
L	Length
M	Mass
$\mathbf{n}$	Normal vector
N	Total number of elements
p	Apparent method order
P	Pressure
q	Flow rate
Q	Heat
r	Radius
R	Dimensionless radius
R_c	Thermal contact resistance
t	Time
$\mathbf{t}$	Tangent vector
T	Temperature
$\mathbf{u}$	Velocity
w	Width
x	x-coordinate
X	Independent experimental variable
y	y-coordinate
z	z-coordinate

Subscripts and Superscripts

$'$	Per unit length
∞	Ambient condition
1	Location 1 of Blanket 1
2	Location 2 of Blanket 1
a	Approximate
C	Capillary
$const$	Constantan
ext	Extrapolated
gap	Spacer gap
gel	Alcogel
hot	Inlet ethanol
i	i^{th} element
ini	Initial value
max	Maximum
$meas$	Measured
$pore$	Pore
ref	Reference
$roll$	Alcogel roll
ss	Steady state condition
w	Hot wire

Abbreviations

ASME	American Society of Mechanical Engineering
AWG	American wire gauge
CGI	Grid Convergence Index

DAQ	Data acquisition
EtOH	Ethanol
HMDZ	Hexamethyldisilazane
JFE	Journal of Fluid Engineering
MOR	Modulus of rupture
NI	National Instruments
NMR	Nuclear magnetic resonance
PDMS	Polydimethylsiloxane
PSD	Pore size distribution
TEOS	Tetraethyl orthosilicate
TMOS	Tetramethyl orthosilicate

CHAPTER I

Introduction

Aerogels, or gels with air-filled pores, are extremely lightweight nanoporous materials which were first produced in 1931 [6]. Aerogels can be created from many materials, though silica aerogels are the most commonly produced and studied. Their physical structure results in unique properties including high specific surface area (500-1200 m^2/g), high porosity (up to 99 %), low density (≈ 0.003 g/cm^3), low thermal conductivity (0.005 W/m·K), low dielectric constant (1.0-2.0), low index of refraction (≈ 1.05), and small pore diameters (20-40 nm) [7]. These properties have generated interest in aerogel for use as the source material in Cherenkov radiation counters, high-capacitance films in multilayer circuit boards, filters for purifying liquids and gases, acoustic insulators, and both transparent and non-transparent thermal insulators [8, 9].

The synthesis of silica aerogel is performed in three basic steps. The first step is gelation, in which silica alcogel, or a wet gel with alcohol in its pores, is produced using the sol-gel process from a silica source, water and catalysts [7]. The second step, aging, involves curing the alcogel in liquid at elevated temperatures for several hours or days. During aging, the gel matrix is strengthened as solids deposit on the necks between pores, preventing cracking or gel shrinkage during the final step, supercritical drying. The effectiveness and speed of aging are heavily dependent on process conditions, such as aging fluid temperature and pH [3]. During supercritical drying, pore liquid is heated and pressurized above supercritical

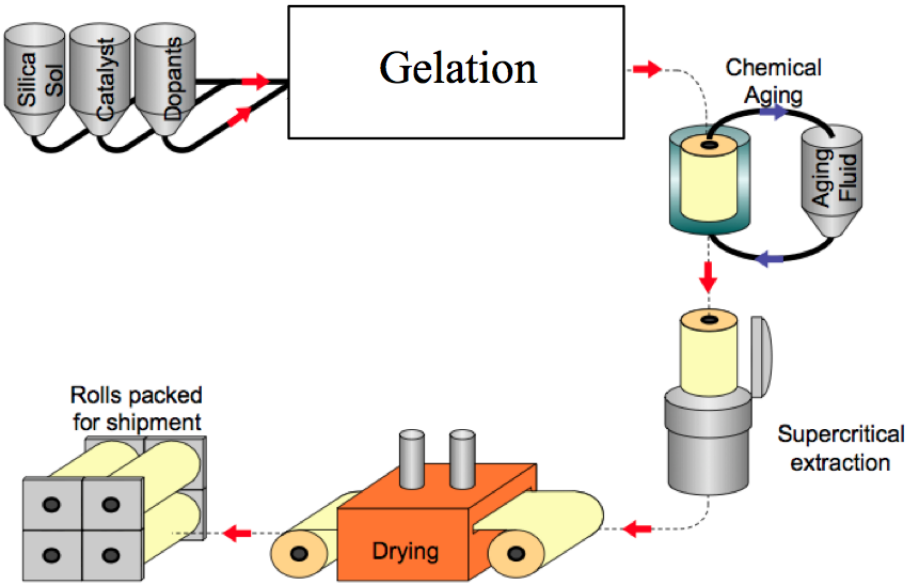

Figure 1.1: Aspen Aerogels' manufacturing cycle

values and then depressurized and cooled, replacing the liquid with gas and thus creating an aerogel. Supercritical drying allows pore liquid to be removed without crossing any phase boundaries, which would give rise to high capillary forces at the liquid-gas interface and cause the gel matrix to collapse, resulting in what is called a xerogel [10].

Despite interest in aerogels, the high cost and complexity of aerogel manufacturing prevented large scale production until the 1980s when aerogels were first used to detect elementary particles in Cherenkov counters [8]. It has been only in the last decade that aerogel has become commercially available as high performance thermal insulation. This thesis research was conducted in coordination with Aspen Aerogels, Inc., a company which has been producing aerogel for thermal insulation since 2001. In their process, aerogel is formed on a fibrous blanket, greatly increasing its strength and flexibility [11]. Figure 1.1 shows the complete manufacturing process, including gelation, aging, and drying, for a blanket of Aspen Aerogels' insulation. This thesis focuses only on the aging step and aims to give insight into potential process improvement targets.

Aging occurs in a cylindrical vessel where the alcogel blanket is heated by a continuous

hot ethanol flow. During this step, the alcogel blanket has been rolled around a mandrel with an insert that keeps gel layers separate and allows for flow between the layers. In comparing bench scale experiments to manufacturing scale aging, Aspen has seen a large disparity in aging time required to achieve a final product which meets the necessary quality standards. Whereas aging takes only 2-3 hours in the lab, times in excess of 10 hours can be required on the manufacturing floor. It is not uncommon for large sections of the blanket to age quickly, leaving only a few areas of the roll which require additional aging. Since there is no difference in the chemistry of these two cases and it is known that aging is thermally dependent, it is proposed that this disparity is a result of the more complex full scale geometry preventing the alcogel blanket from heating quickly and uniformly. For example, winding stresses in the alcogel blanket are higher near the mandrel and may press layers against each other with enough force to block pathways in spite of the separators, preventing the flow hot ethanol. The exterior layers, which experience much lower winding stresses, slouch under their own weight and can press against the walls of the aging vessel, again potentially blocking flow. In addition, a process endpoint is hard to define and therefore alcogel rolls are aged for longer than is necessary to ensure a good final product. A prediction or in-situ measurement of aging completion would help eliminate this added time.

The main goal of this thesis was to develop a better understanding of the alcogel aging process and to identify options for process optimization. To achieve this goal, fluid flow and heat transfer within the aging vessel have been modeled numerically using Comsol Multiphysics, a commercially available computational fluid dynamics (CFD) code. Since geometries involved in the problem include a very wide range of length scales ($<$ mm to m) and local imperfections can impede mass flow and heat transfer phenomena, separate models of various sections within the alcogel roll were used to create a representative description of the aging process. When compared to alcogel roll temperature data, these models provide insight into the mechanisms of alcogel roll heating. In addition, it was necessary to determine the thermal conductivity of silica alcogel since these values were not available in literature.

Since it is well documented that the physical structure of the alcogel changes with aging, the thermal conductivity was measured as a function of aging time. For these experiments, the transient line-source technique was used. A parallel thesis study was also conducted to determine alcogel mechanical properties as functions of aging [12], and property changes and their in-situ measurement have been investigated as process endpoint indicators.

CHAPTER II

Background

2.1 Aerogel Synthesis

There are three basic steps in the production of silica aerogels: gelation, aging, and drying. Gelation creates an alcogel, or wet gel with alcohol filled pores, by use of the sol-gel process from a silica source, water and catalysts. Aging increases alcogel strength and stiffness to prevent shrinkage and cracking during drying. Drying removes pore liquid from the gel structure through a supercritical extraction process, creating an aerogel [7]. In this section, a description of each process is presented and research relevant to property change during aging is summarized.

2.1.1 Gelation

Precursors for alcogels used in aerogel production are generally silicon alkoxides, the two most common being tetramethyl orthosilicate (TMOS) and tetraethyl orthosilicate (TEOS) [7]. TEOS has been used exclusively in this research. TEOS, $Si(OEt)_4$, is synthesized from silicon metal and anhydrous ethyl alcohol as in Eq. 2.1 [13].

$$Si + 4EtOH \overset{catalyst}{\rightarrow} Si(OEt)_4 + 2H_2 \tag{2.1}$$

where Et is an ethyl group, C_2H_5.

Silica alcogel is obtained by the sol-gel process. TEOS is first hydrolyzed, as in Eq. 2.2, creating silanol groups which are then condensed to produce silica linkages and water by-product, as in Eq. 2.3. In most cases, condensation commences before hydrolysis completes and these reactions are concurrent [14].

$$\mathrm{Si(OEt)_4} + 4\mathrm{H_2O} \overset{catalyst}{\rightarrow} \mathrm{Si(OH)_4} + 4\mathrm{EtOH} \tag{2.2}$$

$$n\mathrm{Si(OH)_4} \overset{catalyst}{\rightarrow} (\mathrm{SiO_2})_n + 2n\mathrm{H_2O} \tag{2.3}$$

where n is the number of available silanol groups. The transformation of the viscous liquid to an elastic solid matrix, called gelation, occurs as the clusters of linkages created by condensation grow and connect. It should be noted that the gel point, or the point at which a cluster appears that reaches all surrounding boundaries, is only a statistical event and that there is no change to the chemical evolution of the system [1].

Hydrolysis and condensation are accelerated by acid, base or two-step acid/base catalysis. Use of acid catalysis leads to weak, linear silica linkages whereas base catalysis creates more uniform structures [7]. The two-step acid/base catalysis procedure involves a first step of acid catalyzed hydrolysis with under-stoichiometric amounts of water, producing silanol and condensing some weakly linked silica clusters until the available water has been fully reacted. A second step completes the reaction with a basic catalyst by fully hydrolyzing available TEOS and creating a uniform structure of the weakly linked silica clusters [14]. Use of this procedure allows for reduced condensation times in the second step and good control over the resulting gel structure [7]. Pre-hydrolized TEOS, or TEOS which has undergone the first step of the two-step procedure, is available commercially as Silbond H5 and will be used in the thermal conductivity experiments.

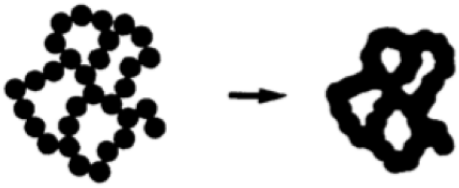

Figure 2.1: Polymerization and coarsening of an alcogel [1]

2.1.2 Aging

The main purpose of aging is to produce a stronger, stiffer alcogel that will not crack or shrink significantly when dried [7]. Additional strength comes from the growth of necks between particles and increased network connectivity, as shown in Figure 2.1. The changing structure experiences an increase in average pore size as smaller pores are filled and a narrowing of the pore size distribution (PSD). There are three main drivers of change during aging: polymerization, syneresis, and coarsening [1].

Polymerization is a continuation of the condensation reactions which began during gelation. Excess hydroxyl groups condense onto the gel structure, creating new bridging bonds and increasing strength and stiffness with time. If there is remaining water and TEOS in the solution, hydrolysis will also continue. Like gelation, the rate of these reactions depends on both temperature and pH [14]. It has been shown that while polymerization has the effect of increasing strength and stiffness with time, condensing silica will eventually begin to fill pores and have a negative effect on porosity. Therefore, an optimum time of aging exists before condensation detrimentally affects the gel structure [15]. This is not a concern in the manufacture of aerogels as the time scale for detrimental polymerization is on the order of days, not hours.

Syneresis is a spontaneous contraction of the gel network resulting in an expulsion of pore fluid. It is often attributed to the increased crosslinking caused by continued condensation reactions. Scherer showed theoretically that the rate of syneresis is dependent on the permeability and viscoelastic properties of the gel network, along with the size of the gel [16].

As crosslinking increases, pulling the gel structure together, a pressure gradient within the pores develops. The flux of fluid J ejected from the pores is given by Darcy's Law, Eq. 2.4.

$$J = \frac{\kappa}{\mu} \bigtriangledown P \tag{2.4}$$

where κ is permeability, μ is fluid viscosity, and $\bigtriangledown P$ is pressure gradient. Shrinkage of the network is inhibited by pore fluid, causing a delay before syneresis starts when the gel network does not yet have the stiffness to create large pressure gradients. There is then a sharp rise in the rate of shrinkage as the modulus of the gel rapidly increases, exerting large stresses on the pore liquid. Eventually, the rising stiffness of the gel ceases further shrinkage. Sample size and geometry are also large factors in determining syneresis since much greater pressure gradients occur at sample boundaries. Accordingly, large samples, or samples with high volume to surface area ratios, will experience less shrinkage than small samples. The theoretical prediction of syneresis presented by Scherer has been supported by experimental data [17].

Coarsening, or Ostwald ripening, is caused by differences in solubility based on surface curvature. Silica is more soluble on convex surfaces than it is on concave surfaces, meaning that silica tends to dissolve from convex particles and reprecipitate on concave necks. This causes considerable neck growth, filling smaller pores and increasing mean pore size and gel strength while decreasing specific surface area [1]. Eventually, over-coarsening will lead to a considerable loss of stiffness and strength in the gel as small particles dissolve and a network of very large pores is created [18]. Since the solubility of silica increases with pH, the rate of coarsening is highest in basic solutions [1].

Several variables in the aging process, and how they affect both the wet and resulting dried gel, have been investigated. The solution in which the gel is aged has been shown to have a significant effect on the development of the porous structure. Aging of gels in water increases polymerization, increasing crosslinking and leading to a broader pore size distribution. Aging

in alcohol pushes the reverse reaction of hydrolysis, called re-esterification, preventing new bridges from forming and favoring coarsening, leading to a narrower pore size distribution [19]. Gels aged in a solution of TEOS and water exhibit increasing average pore size, specific surface area and pore volume with increasing TEOS concentration [15]. In addition, aging in TEOS has been shown to increase gel strength and stiffness, resulting in less shrinkage and lower density in the dried aerogel than gels aged in only water [20]. Aging of alcogels in a solution of hexamethyldisilazane (HMDZ) and TEOS replaces polar Si-OH groups at the gel surface with non-polar Si-CH_3 groups, promoting gel hydrophobicity [21]. The pH of the aging solution has also been shown to have a significant effect on the structural development of the gel network. The solubility of silica increases with at higher pH, accelerating coarsening and resulting in larger pores and a narrower distribution of pore sizes. Condensation reactions also increase at high pH, resulting in a stronger, stiffer network with less gel shrinkage and cracking during drying [22].

Thermal aging has been shown to increase the rate of coarsening, hydrolysis and condensation reactions, allowing for decreased aging times. Smitha et al. measured the linear drying shrinkage, density and average pore size of gels aged for 48 hours at temperatures ranging from 30 °C to 80 °C in a solution of TEOS and isopropanol and then dried under subcritical conditions [2]. Linear drying shrinkage and bulk density are displayed in Figure 2.2 and the average pore size as a function of temperature is given in Figure 2.3. Average pore size experiences a gradual increase with temperature, demonstrating the acceleration of coarsening with temperature. Linear drying shrinkage and bulk density gradually decrease until 60 °C when there is a rapid drop in shrinkage and increase in bulk density. The authors propose that at lower temperatures coarsening dominates, increasing strength and preventing drying shrinkage, keeping densities low. At higher temperatures, a rapid increase in silica condensing on the structure dominates, further increasing the stiffness of the network while also rapidly increasing the weight, and therefore density, of the gel. This result indicates that polymerization and condensation occur at different rates [2].

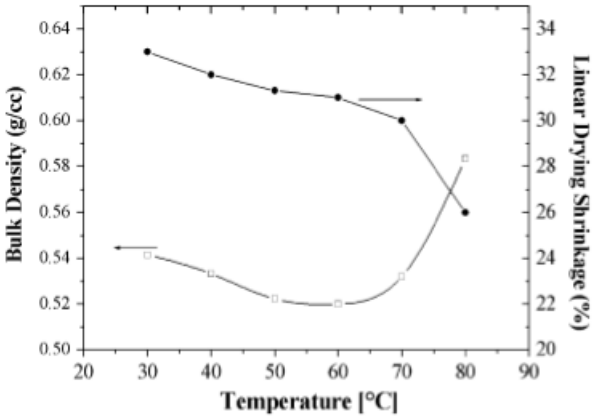

Figure 2.2: Linear drying shrinkage and bulk density of a subcritically dried gel as a function of aging temperature [2]

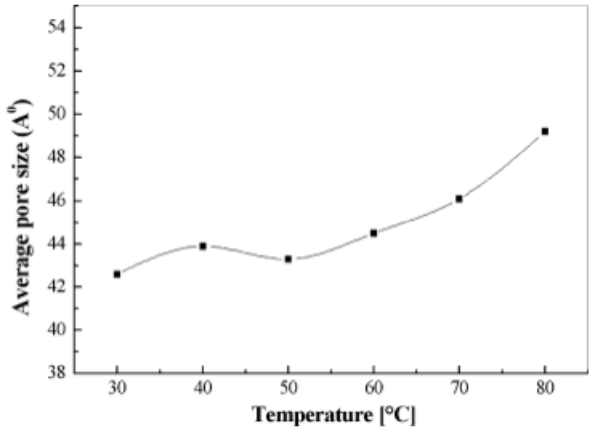

Figure 2.3: Average pore size of a subcritically dried gel as a function of aging temperature [2]

Hæreid et al. measured the shear modulus and modulus of rupture (MOR) of TMOS-based alcogels aged in water and TEOS-based alcogels aged in an ethanol/water mixture for various times at various aging temperatures [18, 23]. In both cases, aging at elevated temperatures resulted in the peak value of shear modulus and MOR occurring sooner in the aging process, indicating a large increase in aging kinetics. For example, the time required to reach the highest shear modulus of 1.6 MPa in the TMOS gels decreased from 132 hours when aged at 40 °C to only 3 hours when aged at 100 °C. In all cases, strength decreased after peaking as the gel over-coarsened [18].

The effect of thermal aging on pore size distribution and average pore size of TEOS-based

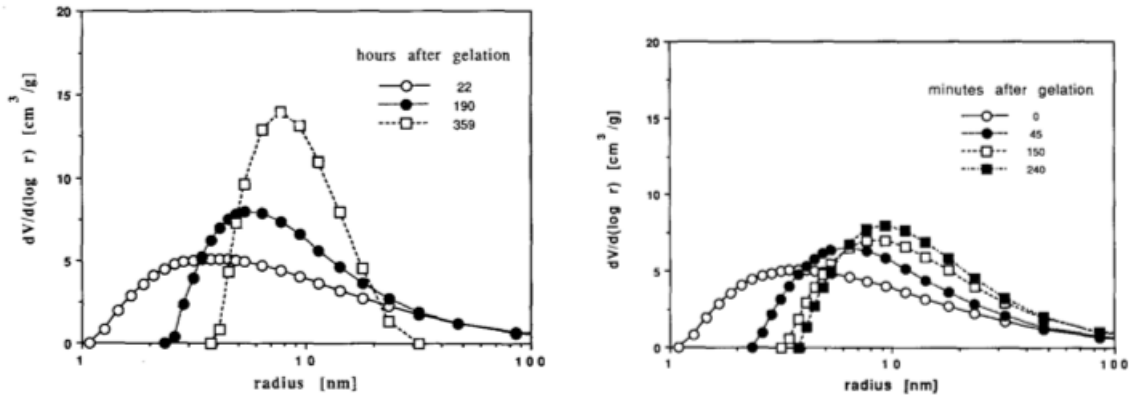

(a) Aging temperature of 30 °C (b) Aging temperature of 60 °C

Figure 2.4: Pore size distribution of TEOS-based alcogel [3]

alcogel was investigated by Davis et al. [3]. Unlike the work done by Smitha et al., data on the pore structure was gathered from the alcogel before drying by use of the Nuclear Magnetic Resonance (NMR) spin-lattice relaxation measurement technique. The PSDs at various times after gelation for gels aged at 303 K and 333 K are presented in Figures 2.4(a) and 2.4(b), respectively. Both plots display a narrowing of the PSD at increased aging times resulting in a more homogeneous gel network. There is also a notable increase in the mean pore size of the gels over time. Davis et al. found that by aging at 333 K, the kinetics of pore structure change were increased by one or two orders of magnitude. This result is explained by increased polymerization and coarsening at increased temperatures [3].

The work of a parallel Master's thesis by Matthew Sherman investigated both the thermal and temporal effects of aging on the yield strength, Young's Modulus, and linear volumetric shrinkage of fiber reinforced silica alcogels. Gels were aged for times between 0 and 24 hours and at temperatures from 50 to 70 °C. Yield strength experienced a slight increase within the first hour of aging before leveling off. Young's Modulus increased rapidly in the first few hours of aging before decreasing slightly and plateauing. The time before modulus change ceased increased with increasing temperature. Linear volumetric shrinkage tests found increased shrinkage with both increasing aging time and temperature. The extent of shrinkage was greatest in samples aged at 60 °C and above. As in the modulus experiments,

linear volumetric shrinkage ceased after a specific time of aging. This time again depended on aging temperature and was related to the plateau times seen in the modulus tests [12].

2.1.3 Drying

Drying of an aerogel involves removing liquid from the pores and replacing it with gas. If done at ambient conditions, pores will experience capillary pressure P_C as given by Eq. 2.5.

$$P_C = -\frac{2\gamma_{LV} cos(\beta)}{r_{pore}} \tag{2.5}$$

where γ_{LV} is liquid-vapor surface tension, β is solid-liquid contact angle, and r_{pore} is the pore radius. Since the pores in silica alcogels are very small, high capillary pressures are exerted on the gel structure [24]. These pressures are capable of collapsing pores and cracking the gel network, resulting in a significantly shrunken xerogel.

To produce high quality aerogels, supercritical drying has been used to avoid high capillary forces and a collapse of the gel network. Supercritical drying involves pressurizing and heating the gel to above the critical point of the pore fluid before returning to ambient conditions, leaving only a gaseous phase in the pores. Above the critical point, the distinction between the liquid and vapor phases disappears, eliminating liquid-vapor surface tension and thus capillary forces [7]. However, shrinkage can still occur due to the restructuring of clusters and consequent weakening of the gel network caused by the very high process temperatures and pressures. [25]. The main purpose of the aging process is to prevent this shrinkage by strengthening the gel network [7].

Direct removal of alcohol through supercritical drying involves very high temperatures (≈270 °C) and pressures (≈12 MPa). Achieving these temperatures and pressures requires a significant amount of time and energy. There are also safety concerns associated with high temperatures, pressures and flammable liquids. To avoid these issues, alcohol can first be exchanged with another liquid which has a lower critical point, such as liquid CO_2. Gels can

then be dried at much lower temperatures (≈40 °C) and pressures (≈8 MPa), allowing for shorter drying times and less drying shrinkage [26].

2.2 Measuring Thermal Conductivity

Thermal conductivity can be determined experimentally using either steady-state or transient methods. Steady-state methods, such as the guarded-hot-plate method and heat flow meter method, involve imposing either a heat flux or a temperature gradient across the test material and measuring the other at steady-state conditions to determine thermal conductivity [27, 28]. These methods are conceptually simple and can be very accurate when carefully designed [29]. However, large temperature gradients are required and the time to achieve steady-state conditions is on the order of hours [27]. Since alcogel exposed to elevated temperatures for extended periods will age, steady-state methods are not suitable.

Transient methods for determining thermal conductivity, while more challenging, use relatively small temperature gradients (≈ 5 °C) and short measurement times (≈ 10 - 60 seconds) [30]. These methods determine thermal conductivity by releasing a known quantity of heat and tracking the transient response of the system. Several such methods exist, including the transient line-source technique, the hot wire method of comparison, and transient spherical-source method, all of which are based on similar theory and achieve similar accuracy [30, 31, 32]. For this reason the simplest and most common such method, the transient line-source technique, will be used to measure the thermal conductivity of alcogels. An ASTM standard exists for measuring the thermal conductivity of plastics by the hot wire method, ASTM D 5930-01, and this standard has guided the experiments in this thesis research [30].

2.2.1 The Transient Line-Source Technique

The transient line-source technique was first suggested by Stalhane and Pyk in 1931 [33]. In 1949, van der Held and van Drunen thoroughly investigated experimental errors and

successfully used the method to determine the thermal conductivity of liquids [34]. Since then, the method has been used to measure the thermal conductivity of silica hydrogels [35, 36], gelatinous food products [37], and polymer melts [38]. Like silica alcogels, these materials undergo chemical changes and thermal degradation when exposed to elevated temperatures for extended times. The method has also used to measure the thermal conductivity of aerogel with good accuracy [39, 40].

The test method involves measuring the transient temperature response of a line-source heater dissipating heat at a known rate that is embedded in a medium of unknown thermal conductivity. On a $ln(t) - T$ plot, the temperature response will have a non-linear initial section followed by a linear section. Figure 2.5(a) is an example of such a heating curve and Figure 2.5(b) shows just the linear section of the same data. The slope of this linear section, along with the rate of heat dissipated from the hot wire, give the thermal conductivity k of the surrounding medium using Eq. 2.6 [30]. Section 2.2.2 provides a derivation of this equation and discusses the assumptions and expected errors.

$$k = \frac{CQ'}{4\pi}\left[\frac{\mathrm{d}T}{\mathrm{d}ln(t)}\right]^{-1} \tag{2.6}$$

where T is wire temperature, t is time, Q' is heat dissipated per unit length of wire, and C is a calibration coefficient. The latter coefficient is determined by measuring the thermal conductivity $k_{measured}$ of a reference material and comparing against literature values k_{ref} as per Eq. 2.7 [30].

$$C = \frac{k_{ref}}{k_{measured}} \tag{2.7}$$

Several physical apparatuses have been developed to serve as both line-source heater and temperature sensor. The most common approach is a rigid, sheathed probe containing a heating element and a thermometer at its center [38, 41]. The advantage of a rigid probe is that it is very durable and can be easily reused. Another approach is to use an exposed, thin

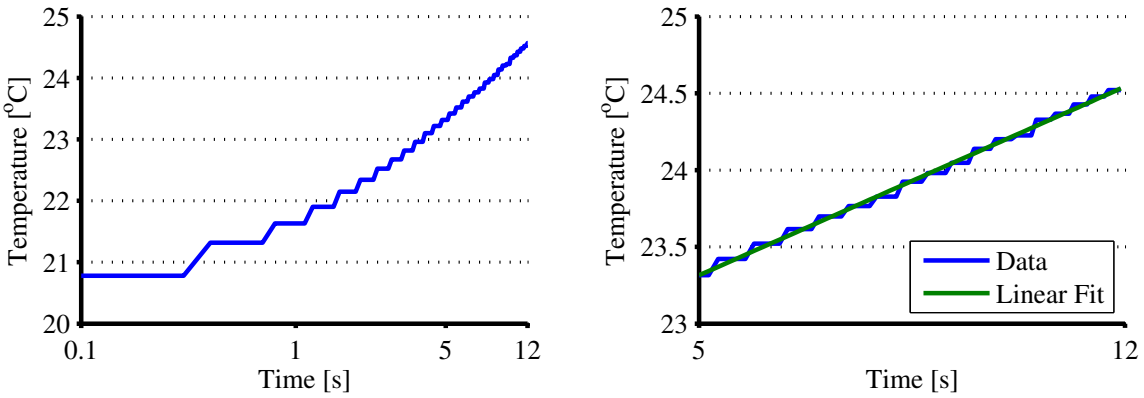

(a) Complete heating curve

(b) Linear section

Figure 2.5: Line-source heater temperature response

wire as a line-source heater and to measure its temperature as a function of wire resistance [42]. This option is simpler to implement and is closer to the theoretical approximations made by the method. Temperature can also be measured by a thermocouple attached at the center of the hot wire, reducing error from three-dimensional heating effects at the wire ends [34]. The latter approach has been used in this thesis.

2.2.2 Derivation

The working equation for the method is derived from the temperature distribution in an infinite medium heated by an infinitely thing, infinitely long, continuous line-source heater. The following is a derivation of that temperature distribution as laid out by Carslaw and Jaeger [43].

Consider an infinite medium with density ρ, specific heat capacity c, thermal conductivity k, and thermal diffusivity α. A time $t = 0$, a quantity of heat Q is released instantaneously at point (x_1, y_1, z_1). For this situation, the differential equation of heat conduction in the medium, Eq. 2.8, is satisfied by Eq. 2.9 for the temperature T at a point (x, y, z).

$$\frac{1}{\alpha}\frac{\partial T}{\partial t} = \frac{\partial^2 T}{\partial x^2} + \frac{\partial^2 T}{\partial y^2} + \frac{\partial^2 T}{\partial z^2} \tag{2.8}$$

$$T(t,x,y,z) = \frac{Q/\rho c}{8(\pi\alpha t)^{3/2}} e^{-[(x-x_1)^2+(y-y_1)^2+(z-z_1)^2]/4\alpha t} \tag{2.9}$$

Now consider an infinite string of point sources running parallel to the z-axis and through point (x_1, y_1) which are separated from each other by distance dz. For simplicity, let $(x_1, y_1) = (0, 0)$ so that the line-source is along the z-axis. Each instantaneous point source now releases heat of strength $Q'dz$ at $t = 0$ where Q' is heat released per unit length. Also, let $r^2 = x^2 + y^2$, where r is the radial distance from the line-source. The temperature distribution in this case can be found by integrating Eq. 2.9 with respect to z, resulting in Eq. 2.10.

$$T(t,r) = \frac{Q'/\rho c}{8(\pi\alpha t)^{3/2}} \int_{-\infty}^{\infty} e^{-[r^2+z^2]/4\alpha t} dz$$

$$T(t,r) = \frac{Q'/\rho c}{8(\pi\alpha t)^{3/2}} e^{-r^2/4\alpha t} \int_{-\infty}^{\infty} e^{-z^2/4\alpha t} dz$$

$$T(t,r) = \frac{Q'/\rho c}{8(\pi\alpha t)^{3/2}} e^{-r^2/4\alpha t} \left[\frac{\pi}{2\sqrt{1/4\alpha t}} erf(z\sqrt{1/4\alpha t}) \right]_{z=-\infty}^{z=\infty}$$

$$T(t,r) = \frac{Q'/\rho c}{4\pi\alpha t} e^{-r^2/4\alpha t}$$

Noting that $\alpha = k/\rho c$, this reduces to:

$$T(t,r) = \frac{Q'}{4\pi k t} e^{-r^2/4\alpha t} \tag{2.10}$$

If Q' is released from the line-source continuously starting at $t = 0$, the temperature distribution at time t can be determined by integrating Eq. 2.10 from 0 to t with respect to time.

$$T(t,r) = \frac{Q'}{4\pi k} \int_0^t \frac{1}{t} e^{-r^2/4\alpha t} dt$$

Substituting $u = r^2/4\alpha t$:

$$T(t,r) = \frac{Q'}{4\pi k} \int_{r^2/4\alpha t}^{\infty} \frac{1}{u} e^{-u} du$$

Note that this integral is the Exponential Integral:

$$\int_{x}^{\infty} \frac{1}{u} e^{-u} du = -Ei(-x)$$

where

$$Ei(-x) = \gamma + ln(x) - x + \frac{1}{4}x^2 + O(x^3)...$$

and $\gamma = 0.5772...$ is Euler's constant. If x is very small, or $r^2/4\alpha t << 1$, then all terms x and higher can be ignored. This leaves:

$$T(t,r) = -\frac{Q'}{4\pi k} Ei(-\frac{r^2}{4\alpha t})$$

$$T(t,r) = \frac{Q'}{4\pi k} ln(\frac{4\alpha t}{r^2}) - \frac{Q'}{4\pi k}\gamma \tag{2.11}$$

The temperature distribution in an infinite medium heated by a continuous line-source is described by Eq. 2.11 [43]. To simplify measurement of k experimentally, Eq. 2.11 can be differentiated with respect to $ln(t)$ [42].

$$\frac{\mathrm{d}T}{\mathrm{d}ln(t)} = \frac{Q'}{4\pi k}$$

$$k = \frac{Q'}{4\pi} \left[\frac{\mathrm{d}T}{\mathrm{d}ln(t)}\right]^{-1} \tag{2.12}$$

Where $\frac{\mathrm{d}T}{\mathrm{d}ln(t)}$ is the slope of the linear section of the $ln(t) - T$ curve when the line-source heater dissipates Q' continuously.

It is important to remember that Eq. 2.12 assumes an infinitely thin, infinitely long heater of no mass in an infinite medium and no contact resistance between the heater and

medium. As none of these assumptions are true in an experimental setup, it is important to determine and include the effects of finite probe size, finite sample size and contact resistance. Blackwell, while considering the use of a rigid line-source probe inserted in a loose drill hole in geologic samples, derived Eq. 2.13 from first principles to solve for the temperature of a heater with finite mass, size and contact resistance in an infinite medium [41].

$$\begin{aligned} T(t) &= \frac{Q'}{4\pi k}[ln(\frac{4\alpha t}{r_w^2}) - \gamma + \frac{2kR_c}{r_w} + \frac{r_w^2}{2\alpha t}\left\{ln(\frac{4\alpha t}{r_w^2}) - \gamma + 1\right. \\ &\quad \left. -\frac{M'c_w\alpha}{r_w k}(n(\frac{4\alpha t}{r_w^2}) - \gamma + \frac{2kR_c}{r_w})\right\} + O(\frac{r_w^4}{\alpha^2 t^2})] \end{aligned} \tag{2.13}$$

where R_c is contact resistance, r_w is heater radius, c_w is specific heat of the heater and M' is mass of heater per unit length. Again, if $r_w^2/2\alpha t << 1$, Eq. 2.13 reduces to:

$$T(t) = \frac{Q'}{4\pi k}\left[ln(\frac{4\alpha t}{r_w^2}) - \gamma + \frac{2kR_c}{r_w}\right] \tag{2.14}$$

When Eq. 2.14 is differentiated with respect to $ln(t)$, Eq. 2.12 remains. Therefore, contact resistance between the heater and medium has no effect on the slope of the linear temperature response and thus no effect on the measured value of thermal conductivity.

Finite sample size leads to edge heating effects which will alter the measured value of thermal conductivity. These edge effects can be eliminated by ensuring that test times are kept small enough to prevent the thermal wave from reaching the sample boundary [44]. An approximation of the maximum allowable test length t_{max} for a sample with minimum dimension δ is provided by Eq. 2.15 [45].

$$t_{max} = \frac{\delta^2}{4\alpha} \tag{2.15}$$

Finite probe size and mass have an effect on the slope of the linear section of the $ln(t) - T$ heating curve. In practice, this slope is corrected by the calibration factor C defined in section 2.2.1. Again, C is the ratio of the published value of a reference material's thermal

conductivity to its measured value. This constant depends only on the probe characteristics and has been found to have no sensitivity to temperature [38].

CHAPTER III

Experimental Methodology and Measurements

Modeling the aging process requires knowledge of the thermophysical properties of fiber-reinforced silica alcogel. Since this information is not available in literature, the properties had to be determined experimentally. A parallel thesis determined the Young's Modulus, yield strength, and linear volumetric shrinkage of fiber-reinforced silica alcogels as functions of aging [12]. This thesis has focused on measuring the thermal conductivity of fiber-reinforced silica alcogels as a function of aging time.

The thermal conductivity measurements were performed using the transient line-source technique, or hot wire method. Background on this technique can be found in Section 2.2. The results of these tests were used in the models described in Chapter IV. Additionally, property changes with aging time were evaluated as a means of monitoring aging progress.

3.1 Methodology

The transient line-source procedure was adapted from ASTM D 5930-01 to fit the specific needs of measuring alcogel thermal conductivity as a function of aging time [30]. Line-source probes were created by attaching a thermocouple to the center of a constantan "hot wire" and were calibrated against polydimethysiloxane (PDMS). Probes were cast into fiber-reinforced alcogel samples aged for various lengths of time at 60 °C. The thermal conductivities of the aged gels were then determined. In some cases, the experiment was performed both before

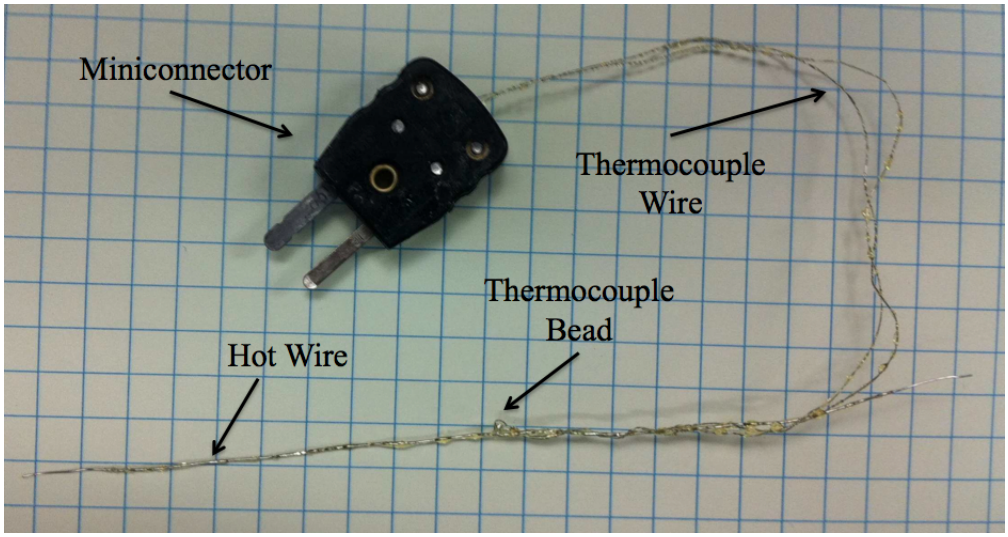

Figure 3.1: Line-source probe for measuring thermal conductivity

and after aging to better illustrate relative trends.

3.1.1 Probe Construction and Calibration

The line-source probes, as shown in Figure 3.1, were J-Type thermocouples attached to line-source heaters. The heaters, or hot wires, were uninsulated 0.381 mm diameter constantan wire cut into strips about 10 cm in length. Constantan was chosen as its electrical resistivity is a weak function of temperature, allowing ohmic heat dissipation from the wire to be accurately calculated despite increasing wire temperatures. Uninsulated 36 AWG iron and constantan wires were spot welded to create the J-Type thermocouples.

To create a probe, a thermocouple bead was soldered to the center of a hot wire using tin/lead solder. Care was taken to ensure that the resulting junction was small and that solder only contacted the thermocouple bead and the hot wire. The three connected wires were dipped in polyurethane multiple times to electrically insulate them from one another, drying for 1 hour between each coat. The individually coated thermocouple wires were wrapped around one side of the hot wire in a spiral and dipped in a final coat of polyurethane to hold all wires in place. All wires were allowed to dry for 24 hours. Wire ends were stripped of coating and a J-Type mini-connector was attached to the thermocouple.

Probes were calibrated in accordance with ASTM D 5930-01 against PDMS [30], a silicone polymer with a well documented thermal conductivity. Each probe was inserted into a $5 \times 2.5 \times 1.25$ cm^3 mold and PDMS (Dow Corning Sylgard 184) was cast around it. Tests were run using the procedure described in Section 3.1.3, with the exceptions that C was assumed to be 1 during calibration and that tests were performed in air, not aging solution. This procedure was repeated on 5 samples of PDMS and the resulting values of thermal conductivity were recorded. The probe's calibration coefficient C was then determined using Eq. 3.1.

$$C = \frac{k_{ref}}{k_{ave}} \tag{3.1}$$

Where k_{ave} is the average measured thermal conductivity of the 5 PDMS samples and k_{ref} is the reference value of PDMS thermal conductivity, 0.16 W/m·K [30]. In total, 17 probes were made with calibration coefficients ranging from 0.78 to 0.88. This range is reasonable and consistent with calibration coefficients in literature [38].

3.1.2 Sample Preparation

Alcogel samples were gelled over a fiberglass batting using Silbond H5, water, ethanol, and ammonium hydroxide. Silbond H5 is a commercially available pre-hydrolyzed silica source from the Silbond Corporation. The ethanol used was 9 to 11% water by volume. In later tests, the water content was measured and found to be 10.4%. Samples were aged in a solution of ethanol and hexamethyldisilazane (HMDZ). The sol-gel and aging solution recipes are given in Table 3.1 and are representative of preparations in literature using an H5 precursor [46].

To prepare a sample, a probe was threaded into a $5 \times 2.5 \times 1.25$ cm^3 piece of the fiberglass batting. The probe and batting were then placed in a plastic mold. The recipe in Table 3.1 was prepared and well mixed. The resulting solution was poured into the mold with the probe and batting and was allowed to gel. Gel times were 3:40 $\pm$10 seconds. The alcogel sample was then removed from the mold and placed in room temperature aging solution to

Table 3.1: Alcogel and Aging Solution Recipes

	Chemical	Percent by Volume [%]
Sol (89 %)	Silbond H5	30
	Ethanol	60
	Water	10
Catalyst (11 %)	Ammonium Hydroxide	6
	Ethanol	94
Aging Solution	HMDZ	8
	Ethanol	92

prevent pore fluid evaporation. A prepared sample can be seen in Figure 3.2. At this point, samples were either tested, aged, or tested and then aged.

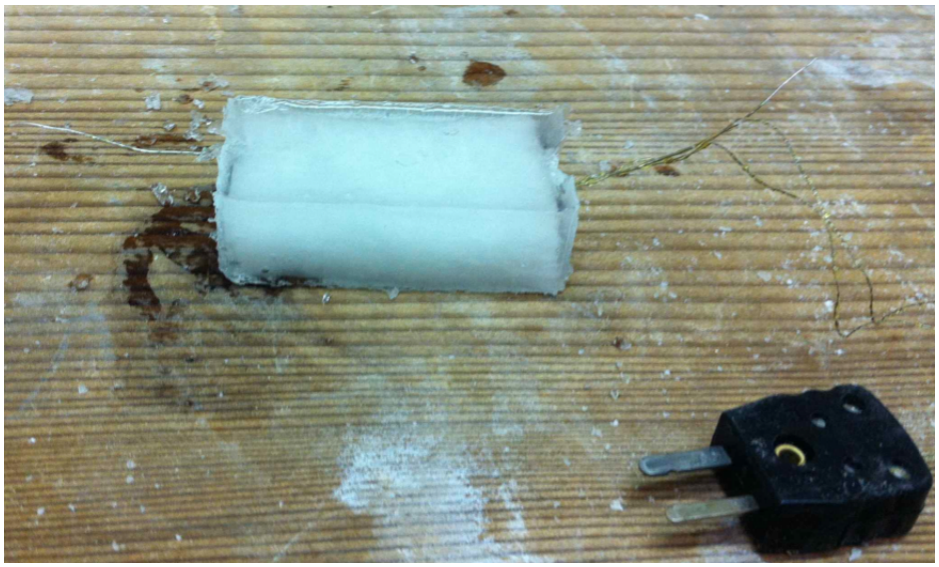

Figure 3.2: Fiber reinforced alcogel sample with line-source probe

Samples to be aged were placed in plastic bags with 150 mL of aging solution. Excess air was removed to reduce buoyancy and bags were heat sealed. Bagged samples were placed in a heated aging bath maintained at 60 ± 1°C and removed after 3, 6 or 24 hours. The aging bath, shown in Figure 3.3, was an insulated 120 L plastic container hooked to a Cole-Palmer Polystat EW-1207-00 Heated Circulating Bath. Deionized water was heated and pumped at a flow rate of 15 L/min to the aging bath and then circulated back to the heater by a gravity drain.

Bags were cooled in room temperature water for 5 minutes to minimize vapor release upon

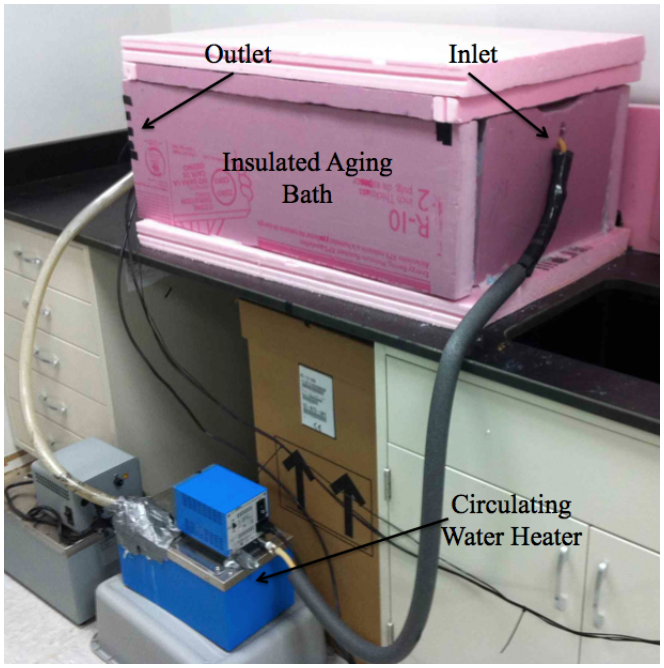

Figure 3.3: Circulating water heated aging bath

opening. Bags were opened and samples were placed in newly mixed, room temperature aging solution. Sample temperatures were allowed to equilibrate for 30 minutes before testing.

3.1.3 Testing

All tests were performed in a room temperature bath of aging solution open the atmosphere. The ends of the line-source heaters were connected by gator clips to an Agilent E3634A DC power supply and National Instruments (NI) 9485 solid state relay, as shown in Figure 3.4. Probe thermocouples were connected to a NI 9211 thermocouple reader. An additional thermocouple was placed in the test bath to record ambient temperature. The solid state relay and thermocouple reader were attached to a NI cDAQ-9174 data acquisition board. NI LabVIEW 2009 was used for solid state relay control and temperature data collection.

During testing, a constant current of 1.125 A was supplied to a line-source probe for 12 seconds. The temperature response of the probe and bath were recorded at a sampling frequency of 100 Hz. The solid state relay then directed current to the next probe and data

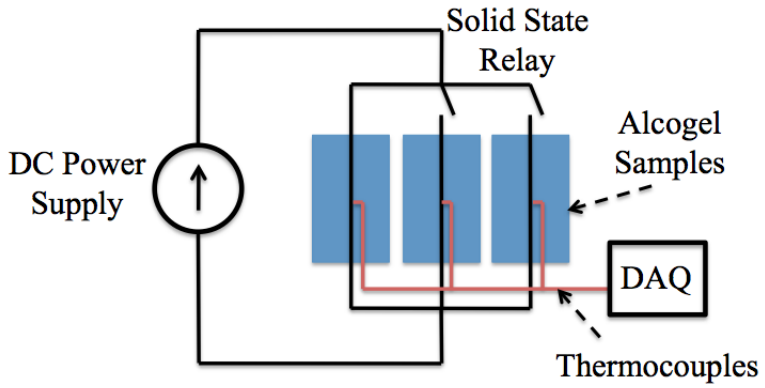

Figure 3.4: Experimental setup

was again collected. In this manner, 3 samples could be tested in rapid succession. After all 3 samples were tested, the system was allowed to equilibrate for 5 minutes. The cycle was then run again. Each sample was tested a total of 3 times to check the consistency of the experimental apparatus.

The thermal conductivity of each sample was determined using Eq 3.2.

$$k = \frac{CQ'}{4\pi}\left[\frac{\mathrm{d}T}{\mathrm{d}ln(t)}\right]^{-1} \tag{3.2}$$

Where C is the calibration coefficient of the probe used, Q' is the heat dissipated per unit length of hot wire, and $\frac{\mathrm{d}T}{\mathrm{d}ln(t)}$ is the slope of the linear section of the transient temperature response plot. Q' was calculated by assuming ohmic heating using Eq. 3.3.

$$Q' = \frac{4I^2\rho_{const}}{\pi d_w^2} \tag{3.3}$$

Where I is the supplied current, ρ_{const} is the electrical resistivity of constantan, and d_w is the diameter of the hot wire. The start of the linear section was determined experimentally by analyzing the temperature response plots of several samples. Linearity in all tests occurred between 3 and 4 seconds. To ensure the start of each slope calculation was well within the linear range, 5 seconds was chosen as the calculation start time. The theoretical maximum

test length, described in Section 2.2.2, was calculated to be about 15 seconds. To again ensure linearity, the calculation end time was chosen as 12 seconds. The slope of the linear section was determined by fitting a line to the data using a least squares fit.

3.1.4 Experimental Uncertainty

The uncertainty associated with the thermal conductivity measurement was determined using the method described by Kline and McClintock [47]. In this method, the overall uncertainty of the measurement is described by a root-sum-square combination of the individual uncertainties in the experiment. The uncertainty δk of the thermal conductivity was calculated using Eq. 3.4.

$$\delta k = \left[\sum_{i=1}^{N} \frac{\partial k}{\partial X_i} \delta X_i \right]^{1/2} \tag{3.4}$$

Where X_i is the i^{th} independent variable associated with the measurement, δX_i is the uncertainty associated with the i^{th} independent variable, N is the total number of independent variables, and k is the thermal conductivity determined by Eq. 3.2. The independent variables and their uncertainties are given in Table 3.2. The measurement uncertainty associated with the thermal conductivity measurement was found to be ±0.008 W/m·K.

Table 3.2: Uncertainties associated with the thermal conductivity experiment

Variable	Symbol	Uncertainty
Current	I	0.0017 A [48]
Temperature Change	∂T	0.05 °C [49]
Calibration Coefficient	C	0.002

3.2 Results and Discussion

A volume averaged calculation was performed to predict the thermal conductivity of the silica alcogel. For the calculation, it was assumed that the gel had a porosity of 95 % and was composed of only silica (k_{Silica} = 1.360 W/m·K) and ethanol (k_{EtOH} = 0.169 W/m·K) [50, 51]. The thermal conductivity of the alcogel was predicted to be 0.230 W/m·K

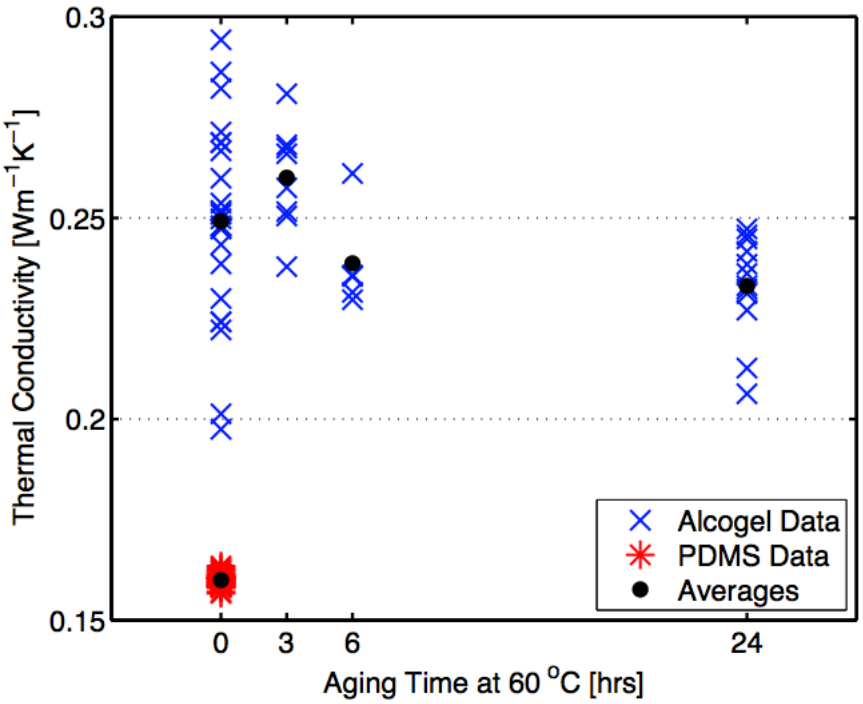

Figure 3.5: Preliminary thermal conductivity results

using Eq. 3.5.

$$k_{gel} = (1 - \phi)k_{Silica} + \phi k_{EtOH} \tag{3.5}$$

The preliminary results of the conductivity experiment are shown in Figure 3.5 and summarized in Table 3.3. The thermal conductivity of an unaged fiber reinforced alcogel is about 0.25 W/m·K, in good agreement with the volume averaged prediction. After aging for 3 hours at 60 °C, thermal conductivity increases slightly before experiencing a 4 % decrease to 0.24 W/m·K at 6 hours. Additionally, the data scatter appears to decrease with increased aging time.

Table 3.3: Summary of preliminary thermal conductivity results

Time Aged [hrs]	Average k [W/m·K]	Standard Deviation
0	0.249	0.024
3	0.260	0.013
6	0.239	0.013
24	0.233	0.013
PDMS	0.160	0.001

The results of the PDMS calibration tests are also displayed in Figure 3.5. These data are shown to give an indication of the uncertainty inherent in the test method. As can be seen, the scatter in the alcogel data is much greater. Data from the mechanical properties experiments also show a similar amount of scatter [12]. The magnitude of this scatter in comparison to the experimental uncertainty caused concern that there was a lack of control in sample preparation. Of particular concern was the storage and time stability of Silbond H5 [52]. Once exposed to a humid atmosphere, Silbond H5 can continue to hydrolyze as it absorbs moisture. This process is slow, but after several weeks or months, continued hydrolysis can result in gels with different starting molecular weights, meaning gels at hour 0 are significantly different from those created weeks earlier. To test if this had occurred, results were separated into populations by date of sample creation. The two largest populations, gelled about 2 months apart, are shown in Figure 3.6. Once separated, there are two distinctly different populations at hour 0, the hump at hour 3 disappears, and there is no longer a significant decrease in scatter with time. The significance of this difference was confirmed by a t-test with a 99 % confidence interval ($p = 0.0059$). The time instability of H5 appears to have a significant effect and should not be ignored.

Data from 8/17/10 to 8/23/10 show no change in thermal conductivity with aging. It is thought that the Silbond H5 used for these tests was many months old and had already significantly hydrolyzed on the shelf. The resulting gels then experienced fewer hydrolysis and condensation reactions during aging, limiting structure and property change. At some point after these tests and before the tests from 10/4/10 to 10/8/10, new H5 was opened.

In the data from 10/4/10 to 10/8/10, gel thermal conductivity remains constant from 0 to 3 hours of aging before rapidly decreasing by 8 % from 3 to 6 hours of aging. The statistical significance of this decrease was supported by a t-test with a 99 % confidence interval ($p = 0.032$).

To eliminate the uncertainty associated with the age of the Silbond H5, new H5 was purchased and tests at all aging times were performed within a week of opening. These

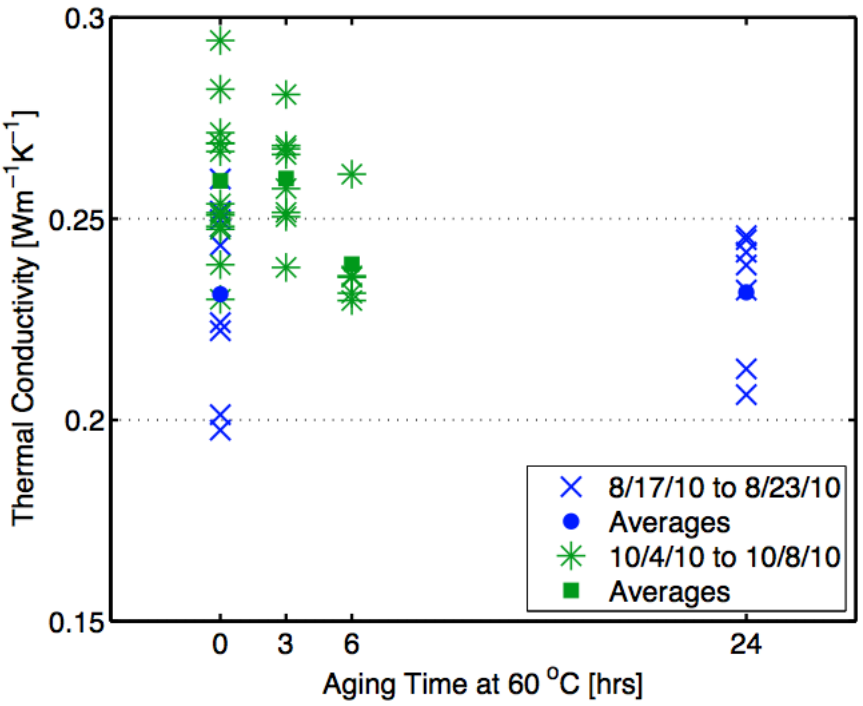

Figure 3.6: Thermal conductivity separated by date of sample gelation

results provide insight into relative changes in thermal conductivity caused by aging. For absolute, repeatable results, future experiments should avoid use of Silbond H5. TEOS based alcogels should instead be created by a carefully controlled two step acid-base catalyzed sol-gel process. Results of the new experiments are shown in Figure 3.7 and summarized in Table 3.4. Gel thermal conductivity again remains constant between 0 and 3 hours of aging before decreasing by 4.8 % between 3 and 6 hours of aging. Gel thermal conductivity then appears to remain constant until 24 hours. The significance of the decrease in gels aged for 6 or more hours was again supported by a t-test with a confidence interval of 85 % ($p = 0.1063$). Data also show a decrease in data scatter between 6 and 24 hours that was shown to be statistically significant by a f-test with a confidence interval of 90 % ($p = 0.059$).

The results indicate that aging decreases the value of alcogel thermal conductivity by 4.8-8.0 %. This change appears to cease after 6 hours of aging, a result that is consistent with the results of the mechanical properties experiments, which found that at an aging temperature of 60 °C property changes were complete after about 6 hours [12]. The data

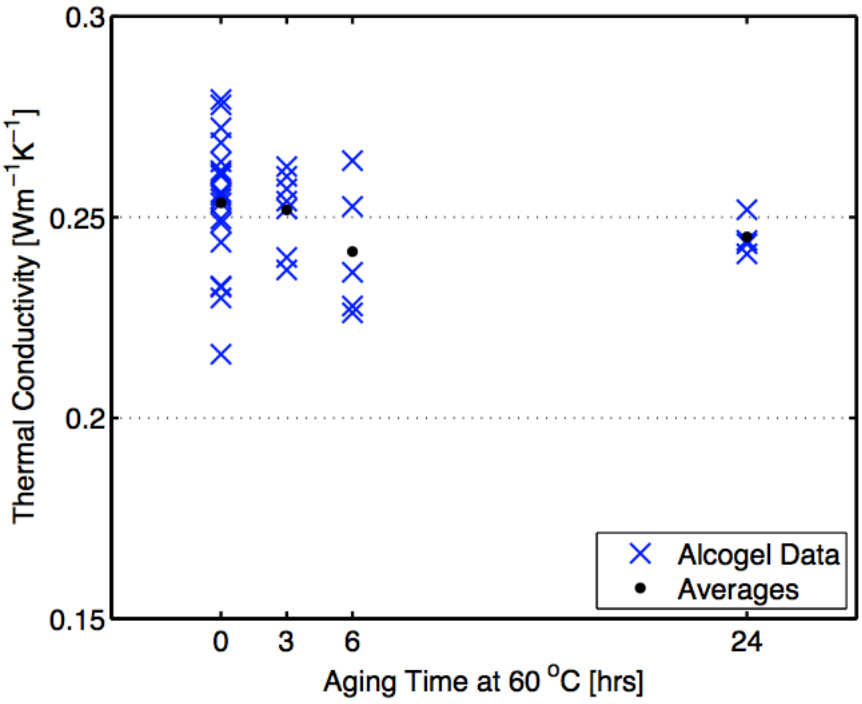

Figure 3.7: Thermal conductivity results using new H5

also show a narrowing in distribution of measured values that occurs between 6 and 24 hours of aging. The narrowing can be explained by the disappearance of irregularities in gel structure with increased aging time.

Table 3.4: Summary of thermal conductivity results using new H5

Time Aged [hrs]	Average k [W/m·K]	Standard Deviation
0	0.254	0.017
3	0.252	0.010
6	0.242	0.016
24	0.245	0.005

The remaining scatter has been attributed to variations in reinforcing fiber density and pattern. Despite having an overall fiber direction, the fiberglass blanket used in the experiments is full of irregularities in both pattern and density. These irregularities are significant and future experiments should work to quantify their effect.

The findings of the thermal conductivity and mechanical properties tests indicate that the thermophysical properties of fiber reinforced alcogel are relatively weak functions of

aging [12]. For this reason, and because of the large range in measured values caused by reinforcing fiber irregularities, monitoring the progress of aging by in-situ property measurement is impractical. A better approach would be to monitor the temperature of the alcogel and use the information on property transformation generated by these experiments to predict aging completion. For example, if a section of blanket has been at 60 °C for 6 hours, the results of these experiments indicate that the gel should be sufficiently aged.

CHAPTER IV

Modeling

In order to accelerate the aging process, its limiting factors must be understood. Currently, the aging of the gel roll is non-uniform, resulting in increased manufacturing times and sections of lower quality final product. Since the chemistry of the process is well understood, these issues are believed to be a result of the gel roll heating non-uniformly. Data from temperature loggers within the blanket support this theory.

Models of ethanol flow and heat transfer within the vessel have been developed to better understand the non-uniform heating of the gel roll. However, a wide range of length scales (0.1 mm to 1 m) and variations in geometries (sections of the rolled blanket slouch in places) prevent the entire vessel from being modeled effectively. Instead, temperature data from the aging vessel have been analyzed for trends and problem areas have been identified. Two models, the Spacer Gap Model and Conduction Model, have been constructed in Comsol Multiphysics 4.0 based on these trends. Together, they help explain how sections of the blanket heat differently and indicate the limitations of the current aging process.

4.1 Aging Vessel Data and Observations

Temperature data was taken from within the aging vessel using temperature loggers dropped on the gel blanket before rolling. All loggers were placed at half the width of the unwound blanket, or half the height in the roll geometry, and at various locations along its

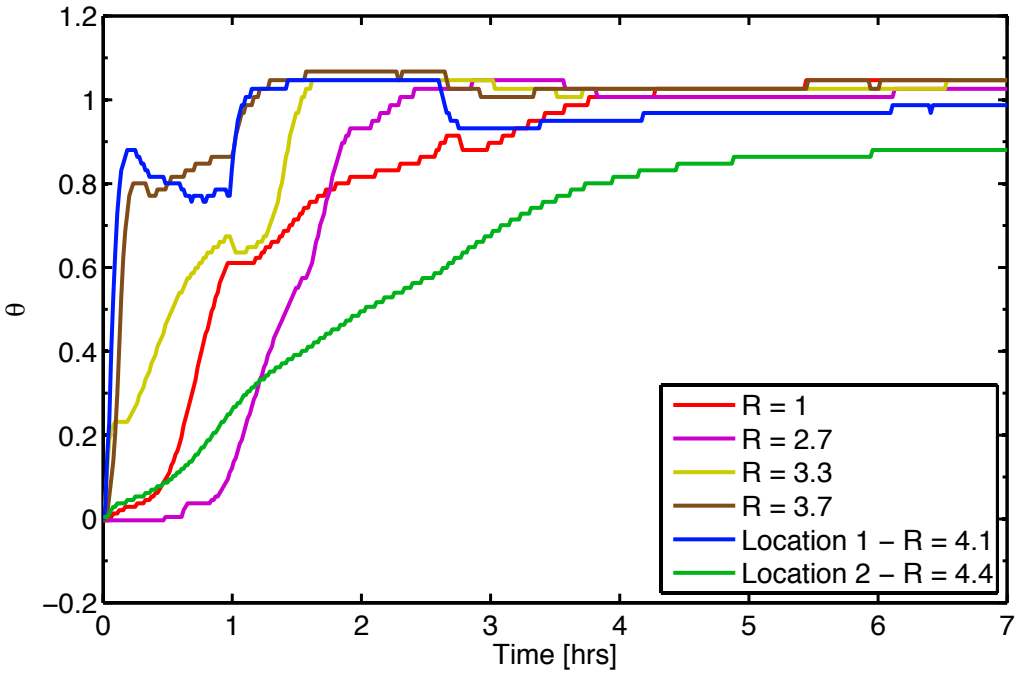

Figure 4.1: Temperature at various locations in Blanket 1

length. Data gathered for two blankets are presented in Figures 4.1 and 4.2. θ is dimensionless temperature and is calculated by Eq. 4.1.

$$\theta = \frac{T - T_{ini}}{T_{hot} - T_{ini}} \tag{4.1}$$

Where T_{ini} is the initial roll temperature and T_{hot} is the temperature of the hot ethanol at the inlet. R is dimensionless radius, given by $R = r/r_{\circ}$, where $r_{\circ}$ is the radius of the innermost point. It should be noted that the azimuthal location of the T-loggers is unknown and therefore two points with similar radii are not necessarily near each other. In both cases, T_{hot} was kept just below the boiling point of ethanol for safety reasons.

It has been proposed that these different rates of heating are caused by blockages in the channels between layers. The inner layers are wound more tightly, pressing against the separator layer. Winding stresses are potentially high enough to partially embed the separator in the gel, effectively decreasing the space between layers and decreasing ethanol flow. In the middle layers, the winding stresses are not very high and the spacing gaps are

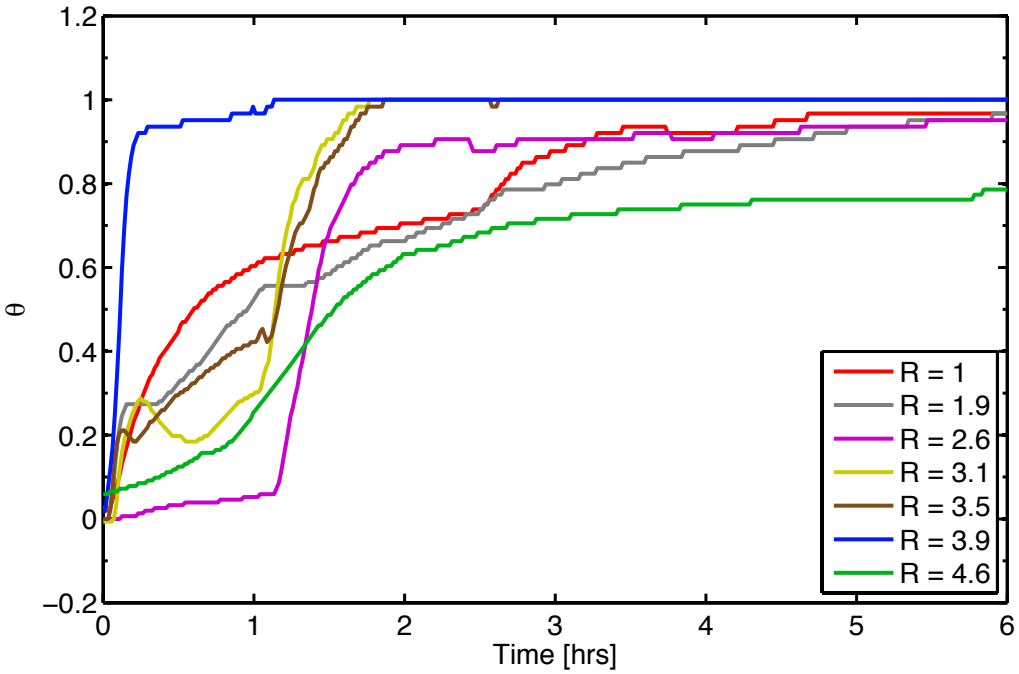

Figure 4.2: Temperature at various locations in Blanket 2

wider. In the outermost layers, the winding stresses are lower still and the layers slump against the walls of the vessel under their own weight. Layers again press against each other, embedding the separator layer in the gel layers and blocking ethanol flow. Blankets removed from the aging vessel often have checkered surface patterns in sections, confirming the presence of separator embedding into the gel.

One of the clearest data trends is that there is a large disparity in the heating times between the two outermost points, locations 1 and 2. In both cases location 1, the blue line, is the quickest to get to temperature whereas location 2, the green line, is the slowest to heat. Radially, these points are close to each other, but they represent the two extremes of heating in the aging vessel. For this reason, it is proposed that location 1 lies in a relatively unblocked channel, meaning that it heats quickly by convection as ethanol flow is unimpeded. At the other extreme, it is conjectured that location 2 lies in a channel which is completely obstructed, meaning it heats purely by conduction from layers closer to the mandrel. Additionally, location 2 reaches a steady state temperature lower than the inlet

ethanol temperature, indicating heat losses to the vessel and its surroundings. To verify this theory, these two situations have been modeled and compared to the experimental data from Blanket 1. The Spacer Gap Model has been created to describe the heating of location 1 and the Conduction Model represents the heating of location 2.

4.2 Spacer Gap Model

The Spacer Gap Model assumes an unobstructed channel between two layers of alcogel. This represents the ideal case in the gel roll, in which the separator works as intended and keeps gel layers separate. Location 1 in Figure 4.1 is hypothesized to lie in such a channel. In this model, hot ethanol flows through the gap between the gel layers due to a pressure drop across the system, heating the entire geometry. Rather than model the geometry of the separator within the open channel, which would have been impractical because of the large range in length scales present, an equivalent channel width was determined assuming Poiseuille flow to match the operating pressure drop and ethanol flow rate in the aging vessel.

4.2.1 Geometry and Material Properties

The Spacer Gap Model geometry is shown in Figure 4.3. Height H is the full height of the gel roll, w_{gel} is half the width of a layer of alcogel, and w_{gap} is the equivalent channel width. There are three subdomains in this model: two identical alcogel subdomains and one spacer gap subdomain. Material properties for the model are presented in Table 4.1. The alcogel subdomains are modeled as porous regions with porosity of 0.95 %. However, as discussed further in section 4.2.3, the permeability of this region is low enough that flow in the alcogel subdomains is negligible. The value of alcogel thermal conductivity was taken from the experimental results and, because conductivity was found to be a weak function of aging, was treated as a constant. All other thermophysical properties were taken to be that of the ethanol within the pores.

The spacer gap subdomain was treated as a region of ethanol. The width of this sub-

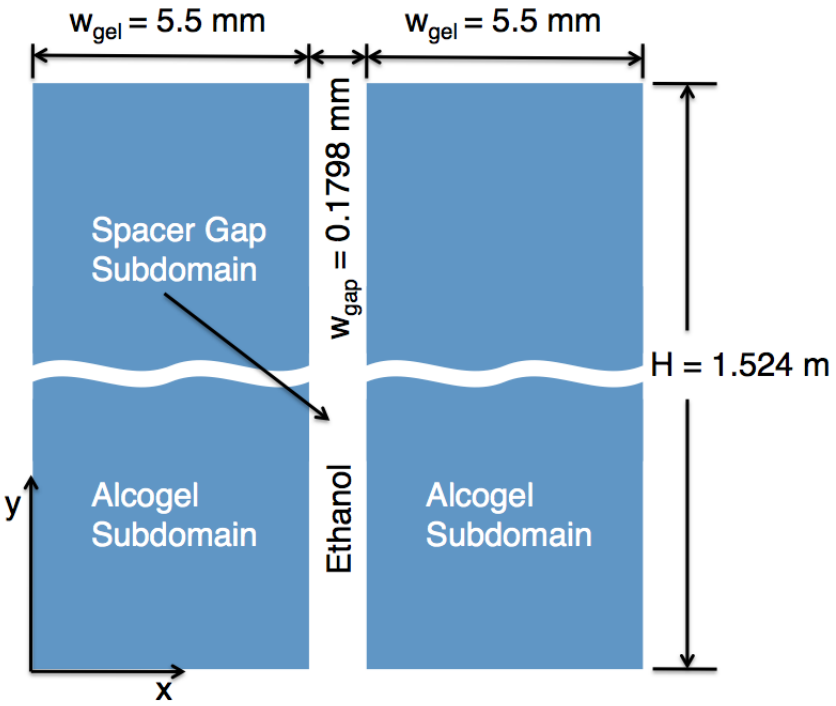

Figure 4.3: Representative geometry of the Spacer Gap Model

domain was calculated to match the operating pressure drop ΔP and flow rate q assuming Poiseuille flow as in Eq. 4.2.

$$q' = \frac{{w_{gap}}^3}{12\mu_{EtOH}} \frac{dP}{dy} \tag{4.2}$$

Where q' is flow rate per unit depth, μ_{EtOH} is fluid viscosity of ethanol, and $\frac{dP}{dy}$ is pressure gradient down the channel. Assuming that all flow through the aging vessel passes through spacer gaps, then q' can be approximated as

$$q' = \frac{q}{L_{Roll}}$$

where L_{Roll} is the total length of the unwound roll, or the total depth of the spacer gap. In addition, a linear pressure gradient has been assumed, so

$$\frac{dP}{dy} = \frac{\Delta P}{H}$$

Table 4.1: Spacer Gap Model material properties [4], [5]

Property	Ethanol	Alcogel
k [W/m·K]	$0.219 - 1.22 \times 10^{-4}T - 1.78 \times 10^{-7}T^2$	0.23
μ [Pa·s]	$0.0742 - 6.17 \times 10^{-4}T + 1.74 \times 10^{-6}T^2 - 1.66 \times 10^{-9}T^3$	
ρ [kg/m^3]	$475 + 4.71T - 0.0176T^2 + 1.84 \times 10^{-5}T^3$	
c [J/kg·K]	$4012 - 18.7T + 0.0451T^2$	
κ [m^2]	N/A	1×10^{-18}
ϕ	N/A	0.95

Rearranging Eq. 4.2 and including the above assumptions, the width of the spacer gap is given by Eq. 4.3.

$$w_{gap} = \left[\frac{12\mu_{EtOH}qH}{\Delta P L_{Roll}}\right]^{1/3} \tag{4.3}$$

4.2.2 Governing Equations

The incompressible Navier-Stokes equations were used to model fluid flow in the spacer gap domain. The continuity and momentum equations are given in Eq. 4.4 and 4.5, respectively [4].

$$\nabla \cdot \mathbf{u} = 0 \tag{4.4}$$

$$\rho\frac{\partial \mathbf{u}}{\partial t} + \rho(\mathbf{u} \cdot \nabla)\mathbf{u} = -\nabla P + \mu\nabla^2\mathbf{u} + F \tag{4.5}$$

Where $\mathbf{u}$ is fluid velocity, F is a body force, μ is dynamic viscosity, P is pressure, and ρ is density. The Brinkman equations, given in Eq. 4.6 and 4.7, were used to model flow in the porous alcogel subdomains [4]. The Brinkman equations are essentially an extension of Darcy's Law that includes a viscous transport term.

$$\nabla \cdot \mathbf{u} = 0 \tag{4.6}$$

$$\frac{\rho}{\phi}\frac{\partial \mathbf{u}}{\partial t} + \frac{\mu}{\kappa}\mathbf{u} = -\nabla P + \frac{\mu}{\phi}\nabla^2\mathbf{u} + F \tag{4.7}$$

Where ϕ is gel porosity.

Since the gel roll heats on the order of minutes to hours, the start-up transient before flow

becomes fully developed is very small in comparison. Flow has therefore been assumed fully developed and steady over the course of the heating process. In addition, external body forces acting on the ethanol are assumed negligible. These assumptions simplify Eq. 4.5 and 4.7 to Eq. 4.8 and 4.9, respectively.

$$\rho(\mathbf{u} \cdot \nabla)\mathbf{u} = -\nabla P + \mu \nabla^2 \mathbf{u} \tag{4.8}$$

$$\frac{\mu}{\kappa}\mathbf{u} = -\nabla P + \frac{\mu}{\phi}\nabla^2 \mathbf{u} \tag{4.9}$$

Solving the flow problem in this manner significantly decreases computation times, since the flow field is resolved only once.

Boundary conditions for the flow problem are summarized in Table 4.2. The operating pressure drop ΔP was assumed from inlet to outlet. Symmetry was assumed at the center of the gel layer, and thus a symmetry boundary condition was present at the external edges of the alcogel subdomains. Continuity was assumed at internal boundaries between subdomains.

Table 4.2: Spacer Gap Model flow boundary conditions

Boundary	Description	Equation
$y = 0$	Pressure	$P = \Delta P$
$y = H$	Pressure	$P = 0$ Pa
$x = 0, 2w_{gel} + w_{gap}$	Symmetry	$\mathbf{u} \cdot \mathbf{n} = 0$, $\mathbf{t} \cdot (-P\mathbf{I} + \frac{\mu}{\phi}(\nabla \mathbf{u} + (\nabla \mathbf{u})^T))\mathbf{n} = 0$

The Heat Equation, Eq. 4.10, was solved to get the temperature T in the geometry.

$$\rho c \frac{\partial T}{\partial t} + \rho c \mathbf{u} \cdot \nabla T = k \nabla^2 T \tag{4.10}$$

Where ρ is density and c is specific heat capacity. Unlike the flow problem, the heat transfer problem was solved transiently to get the temperature field as a function of time.

The boundary conditions for the heat transfer problem are given in Table 4.3. The temperature at the inlet of the channel was taken as the temperature of the hot ethanol

pumped into the aging vessel. At the outlet, heat was allowed to leave only by convection. As in the flow problem, symmetry was assumed at the exterior boundaries of the alcogel subdomains (the center of the gel layers). At all internal boundaries, continuity was again imposed. For the initial condition, temperature throughout the geometry was T_{ini}, the initial temperature of Blanket 1.

Second-order Lagrange elements were used for both the flow and heat transfer problems [4]. First, the flow problem was solved for the velocity field using a stationary solver. All material properties were evaluated at T_{hot}, the temperature of the hot ethanol. Once the velocity field was resolved, the temperature field was solved using a time dependent solver. The generalized-α time stepping method was used to solve for the temperature from 0 out to 2400 seconds in steps of 10 seconds.

Table 4.3: Spacer Gap Model heat transfer boundary conditions

Boundary	Description	Equation
$y = 0$	Temperature	$T = T_{hot}$
$y = H$	Convective Outflow Only	$\mathbf{n} \cdot \nabla T = 0$
$x = 0, 2w_{gel} + w_{gap}$	Symmetry	$\mathbf{n} \cdot \nabla T = 0$

4.2.3 Results

The velocity profile captured in the spacer gap subdomain is given in Figure 4.4. This profile was taken at half the height of the roll, which is the location of interest. The velocity profile is parabolic, as would be expected in a parallel plate geometry. The flow develops rapidly and therefore this profile is representative of the velocity profile over almost the entire height of the spacer gap. The velocity field in the gel subdomains was also calculated, but the extremely low permeability and small pressure gradients resulted in maximum velocities on the order of 10^{-9} m/s, a full 8 orders of magnitude less than the velocities in the spacer gap.

Figure 4.5 gives the average temperature of the entire geometry (spacer gap and gel layers) as a function of time. As shown, the entire geometry reaches the inlet ethanol temperature

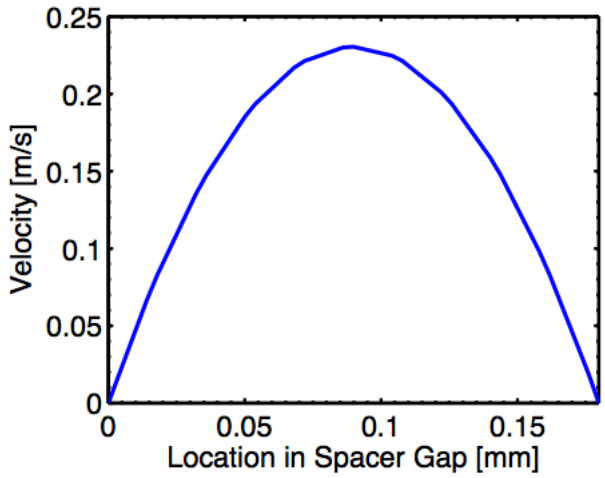

Figure 4.4: Velocity profile in the spacer gap subdomain.

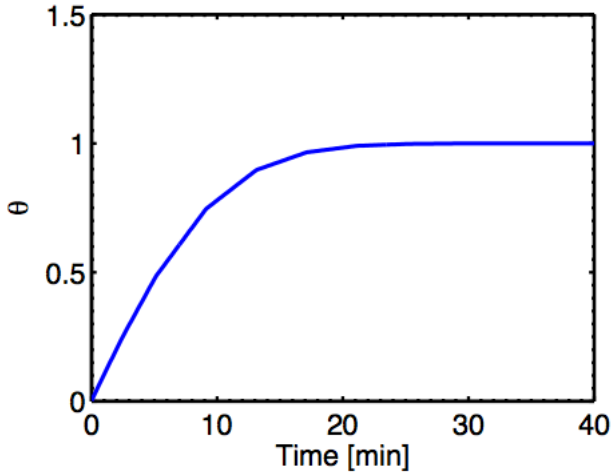

Figure 4.5: Average gel roll temperature.

in about 20 minutes. This finding suggests that if the entire alcogel roll had unobstructed channels, process temperatures could be achieved relatively quickly.

Figure 4.6 gives an idea of how the gel layers heat. Hot ethanol flowing from the inlet is cooled significantly as it passes over the alcogel layers, resulting in much cooler ethanol reaching the top in the initial stages of the process and thus heating the gel roll from the bottom up. The heating of the gel roll is limited by the width of the spacer gap in this manner. As the spacer gap gets smaller, this cooling effect should be larger and the time before hot ethanol reaches the top will increase.

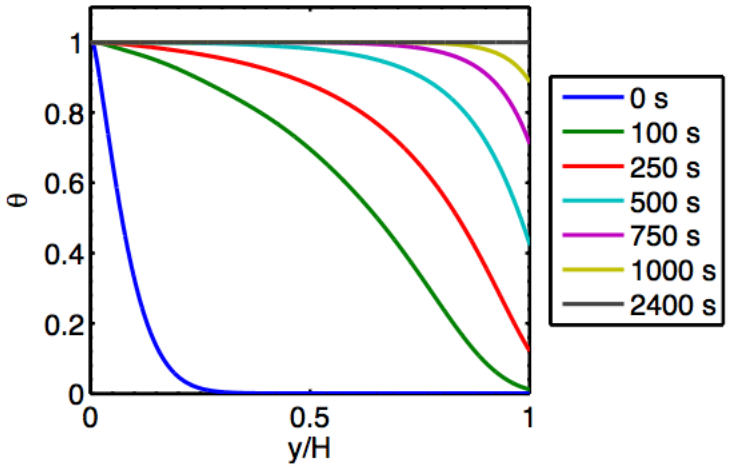

Figure 4.6: Temperature of the center of the spacer gap at various times.

The transient temperature response at the point of interest (half the height of the roll and at the center of the spacer gap) along with the corresponding data from the aging vessel are given in Figure 4.7. The model provides a good match to the data for the first ten minutes, at which point the two lines diverge. The aging vessel data plateaus at $\theta = 0.8$ before reaching $\theta = 1$ at about 1 hour. The model continues to the hot ethanol temperature quickly before plateauing. While there is clearly some effect that the simplified model does not capture in the heating of the gel roll, the close match in heating curve in the initial section suggests that the gap at location 1 is unobstructed.

4.2.4 Mesh Independence Studies

The preceding solutions were found using a mesh of 100,000 (10 by 10,000) quad elements in the spacer gap subdomain and 126,054 triangular elements in the gel subdomains. The critical mesh is in the spacer gap subdomain as the boundary layer of the flow must be captured to accurately predict gel heating. For this reason, the sensitivity of the solution to spacer gap mesh density has been investigated using the American Society of Mechanical Engineering (ASME) Journal of Fluids Engineering (JFE) Grid Convergence Index (CGI) method [53]. The CGI method is summarized below.

First, a representative cell size h is defined based the total number of elements N in the

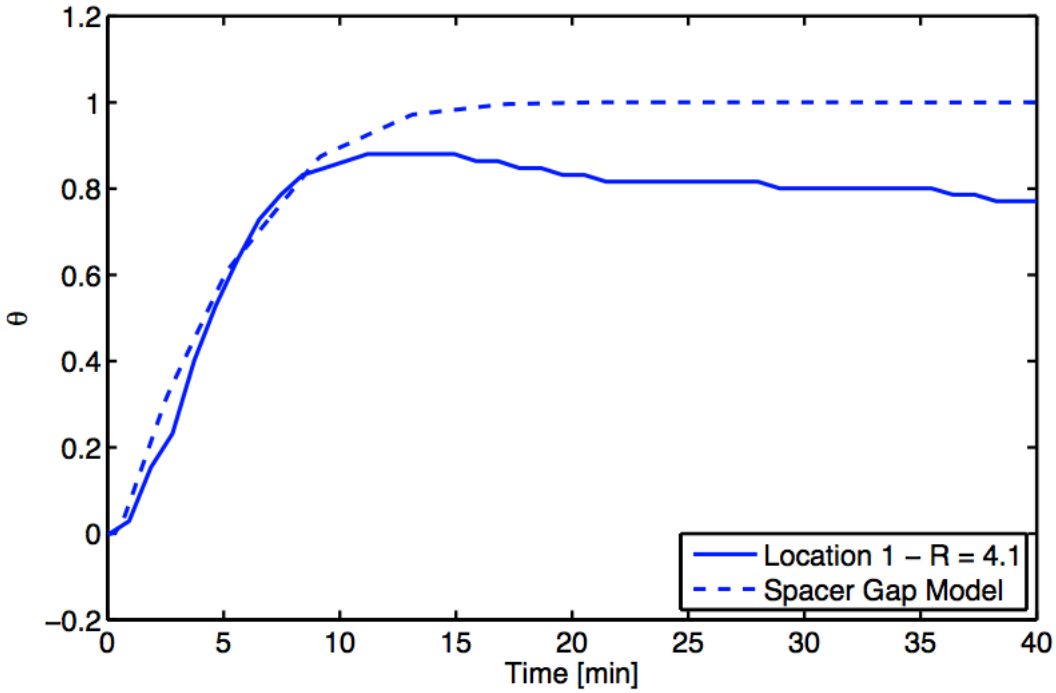

Figure 4.7: Spacer Gap Model results compared to aging vessel temperature data

spacer gap and the sum of the element areas ΔA using Eq. 4.11.

$$h = \left[\frac{1}{N} \sum_{i=1}^{N} \Delta A_i \right]^{1/2} \tag{4.11}$$

The subscript i denotes the i^{th} element.

Next, three significantly different meshes are created such that the ratios of their representative cell sizes follow Eq. 4.12, 4.13, and 4.14.

$$h_1 = h_{fine} < h_2 = h_{medium} < h_3 = h_{coarse} \tag{4.12}$$

$$R_{21} = \frac{h_2}{h_1} \geq 1.3 \tag{4.13}$$

$$R_{32} = \frac{h_3}{h_2} \geq 1.3 \tag{4.14}$$

In addition, these three meshes have element totals of N_1, N_2, and N_3. Note that mesh 2

was used for the solutions in the preceding sections, such that $N_2 = 100,000$.

Simulations are run using all three grids and key variables are determined. For example, if variable ψ is a critical outcome of the simulation, its solution on meshes 1, 2, and 3 is stored as ψ_1, ψ_2, and ψ_3 respectively. The apparent order p of the method is then calculated using Eq. 4.15.

$$p = \frac{1}{ln(R_{21})} \left| ln|\varepsilon_{32}/\varepsilon_{21}| + q(p) \right| \tag{4.15a}$$

$$q(p) = ln\left(\frac{R_{21}^p - s}{R_{32}^p - s}\right) \tag{4.15b}$$

$$s = 1 \cdot sign(\varepsilon_{32}/\varepsilon_{21}) \tag{4.15c}$$

Where $\varepsilon_{32} = \psi_3 - \psi_2$ and $\varepsilon_{21} = \psi_2 - \psi_1$. Eq. 4.15 can be solved using a fixed point iteration where the initial guess assumes $q(p) = 0$.

Extrapolated values for ψ can now be calculated using Eq. 4.16 and Eq. 4.17.

$$\psi_{ext}^{21} = \frac{R_{21}^p \psi_1 - \psi_2}{R_{21}^p - 1} \tag{4.16}$$

$$\psi_{ext}^{32} = \frac{R_{32}^p \psi_2 - \psi_3}{R_{32}^p - 1} \tag{4.17}$$

The approximate relative error, extrapolated relative error, and fine grid convergence index can be calculated using Eq. 4.18, 4.19, and 4.20 respectively.

$$e_a^{21} = \left| \frac{\psi_1 - \psi_2}{\psi_1} \right| \tag{4.18}$$

$$e_{ext}^{21} = \left| \frac{\psi_{ext}^{21} - \psi_1}{\psi_{ext}^{21}} \right| \tag{4.19}$$

$$GCI_{fine}^{21} = \frac{1.25 e_a^{21}}{R_{21}^p - 1} \tag{4.20}$$

The two errors, the grid convergence index and the method order should be reported to indicate the numerical uncertainty associated with the calculation.

The variables of interest chosen for this model were the velocity magnitude at the middle of the spacer gap (ψ_A), at a quarter of the width of the spacer gap (ψ_B), and at an eighth the width of the spacer gap (ψ_C). All of these points were taken at half the height of the geometry, $H/2$. A summary of the results, errors, method orders, and the grid convergence indexes are given in Table 4.4. The findings of the study indicate that the uncertainty caused by the mesh size is very low.

Table 4.4: Mesh independence study results for the Spacer Gap Model

	ψ_A	ψ_B	ψ_C
N_1, N_2, N_3	182252, 100000, 54873	182252, 100000, 54873	182252, 100000, 54873
R_{21}	1.35	1.35	1.35
R_{32}	1.35	1.35	1.35
ψ_1	0.230446	0.172845	0.100829
ψ_2	0.230447	0.172845	0.100830
ψ_3	0.230448	0.172846	0.100830
p	1.1342	1.2590	1.5381
ψ_{ext}^{21}	0.230444	0.172844	0.100829
e_a^{21}	0.000329 %	0.000329 %	0.000315 %
e_{ext}^{21}	0.000811 %	0.000716 %	0.000537 %
GCI_{fine}^{21}	0.00101 %	0.000896 %	0.000671 %

4.3 Conduction Model

The Conduction Model assumes that all channels between points locations 1 and 2 are obstructed. This assumption means that a 3 cm wall of alcogel lies between the two points and that location 2 heats by conduction from location 1. Additionally, the temperature at location 2 never reaches the inlet ethanol temperature, implying some heat loss to the aging vessel and its surroundings. The Conduction Model imposes a heat loss boundary condition to match this lower steady state temperature at location 2 and also investigates the effect of eliminating this heat loss on blanket heating times.

4.3.1 Geometry and Material Properties

A representative geometry of the Conduction Model is given in Figure 4.8. The geometry has been treated as one dimensional since the width of the alcogel wall is significantly less than the total height of the gel blanket.

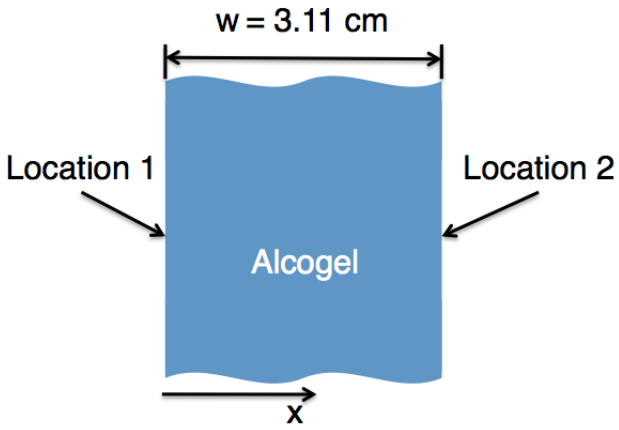

Figure 4.8: Representative geometry of the Conduction Model

The alcogel wall has been modeled as a solid with the density and specific heat capacity of ethanol. The thermal conductivity of the alcogel is given as a constant. The relevant material properties are given in Table 4.5.

Table 4.5: Conduction Model material properties [4]

Property	Alcogel
k [W/m·K]	0.23
ρ [kg/m^3]	$475 + 4.71T - 0.0176T^2 + 1.84 \times 10^{-5}T^3$
c [J/kg·K]	$4012 - 18.7T + 0.0451T^2$

4.3.2 Governing Equations

The Heat Equation was simplified and used to get the temperature T in the geometry. Noting that there is no flow in the geometry ($\mathbf{u} = 0$), Eq. 4.10 reduces to Eq. 4.21.

$$\rho c \frac{\partial T}{\partial t} = k \nabla^2 T \tag{4.21}$$

The boundary equations are given in Table 4.6. The temperature of the left boundary was given as a step function to match the behavior of location 1 in Blanket 1. The temperature at this point rises quickly from the initial temperature to $\theta = 0.8$. For this reason, the temperature of the left boundary began at $\theta = 0.8$ in the simulation and, 48 minutes later, increased to $\theta = 1$ gradually over the course of 4 minutes. For the step, the COMSOL function flc1hs was used. This function is a Heaviside function that has a gradual step after a specified delay. The right boundary was modeled in one of two ways. First, the simulation was run with a convective heat loss boundary condition. The steady state temperature difference was taken between location 2 and the rest of Blanket 1 and an average heat transfer coefficient, $\bar{h}$, was determined using in Eq. 4.22 to be 0.89 W/m·K.

$$\bar{h}(T - T_\infty) = -k\frac{\partial T}{\partial x} \tag{4.22}$$

Where T_∞ is the ambient temperature (assumed to be 20 °C). Note that at steady state $\frac{\partial T}{\partial x}$ can be assumed to be linear with reasonable accuracy. Eq. 4.22 can now be reduced to Eq. 4.23.

$$\bar{h}(T_{2,ss} - T_\infty) = -k\frac{T_{1,ss} - T_{2,ss}}{w} \tag{4.23}$$

Where $T_{1,ss}$ and $T_{2,ss}$ are the steady state temperatures at locations 1 and 2, respectively. The simulation was also run with a thermally insulated boundary on the right to investigate the effects of insulation on the heating time.

Table 4.6: Conduction Model boundary conditions

Boundary	Description	Equation
$x = 0$	Temperature	$\theta = 0.8 + 0.2flc1hs(t - 2880, 240)$
$x = w$, Case 1	Convective Heat Loss	$\bar{h}(T - T_\infty) = -k\frac{\partial T}{\partial x}$
$x = w$, Case 2	Thermal Insulation	$k\frac{\partial T}{\partial x} = 0$

Second-order Lagrange elements were used in both simulations. The initial temperature in the geometry was T_{ini}. The generalized-α time stepping method was used to solve for the temperature field from 0 out to 24480 seconds (6.8 hours) in steps of 10 seconds.

4.3.3 Results

Figure 4.9 shows the results from the right boundary of the one-dimensional Conduction Models and the data from location 2 of Blanket 1. The results of both simulations match the heating time of location 2 fairly well. Both the aging vessel data and the results of the heat loss model take slightly over 3 hours to achieve their final temperature of about $\theta = 0.8$. However, the model does not capture the effects that cause the abrupt changes in the aging vessel data's slope at about 1.5 and 2.5 hours. The temperature on the right boundary of the thermally insulated Conduction Model takes about the same time to plateau; however, it reaches a higher temperature of $\theta = 1$. On the way, the insulated model reaches $\theta = 0.8$ steady state temperature of location 2 in just under 3 hours.

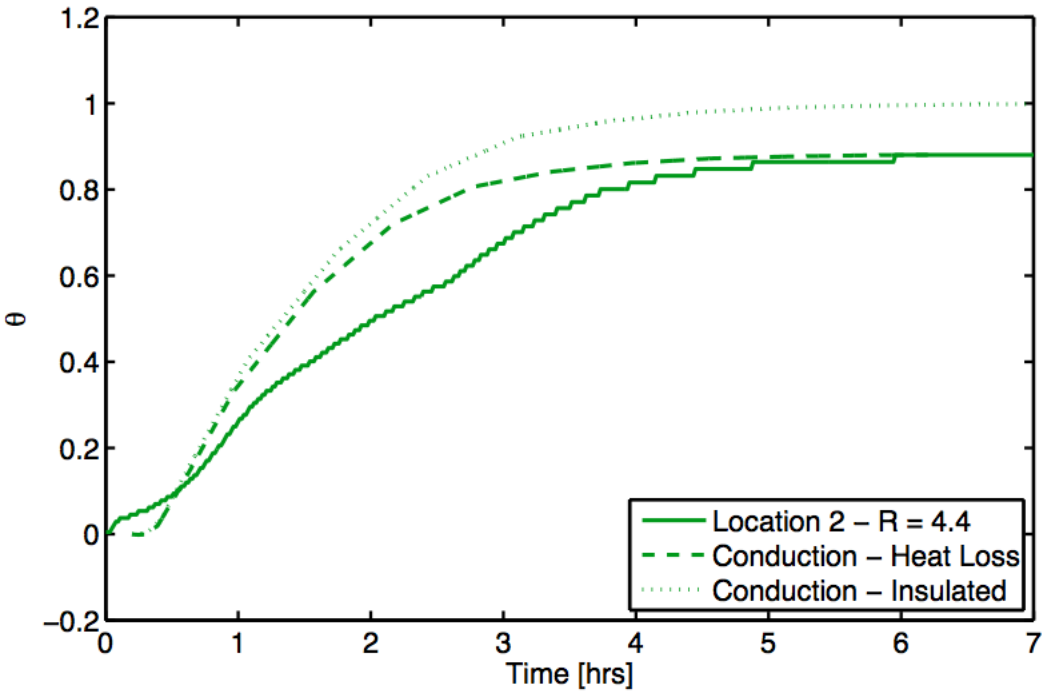

Figure 4.9: Conduction Model results compared to aging vessel temperature data

Mesh independence studies are detailed in Section 4.2.4. The solution was found to be grid independent.

4.4 Discussion

A summary of the modeling results is presented in Figure 4.10. All models match the corresponding data well in regards to heating times, however there are some heating behaviors that are not captured. Some of the discrepancies between the models and data are likely due to lack of information available on model inputs. For example, the exact locations of the temperature loggers were not known while data was being taken; the locations given in this chapter were best estimates. There is no indication that locations 1 and 2 lie in the same direction azimuthally, meaning that it is possible that the radial location 3 cm in and on the same azimuth as location 2 behaves entirely differently. Additionally, the aging vessel is not uniform in the vertical plane. The weight of the rolled blanket likely causes significant variations in geometry towards the bottom of the vessel where there are much higher compressive forces. The effect of the gel's weight on the geometry is not understood and has therefore been ignored. Despite the simplifications used in both the Spacer Gap Model and the Conduction Models, both models match the aging vessel data reasonably well. Location 1 most likely lies in an unobstructed gap, receiving hot ethanol flow, while location 2 lies in a section of alcogel blanket lacking ethanol flow, heating mainly by conduction. These findings are an indication that the separator layer is not accomplishing its intended objective, which is to keep gel layers separate. Instead, layer separation appears to much more dependent on location in the aging vessel. The extent to which the separator can embed into the alcogel under the compressive stresses found near the mandrel and vessel wall is great enough that gel layers can press against each other, obstructing ethanol flow.

The results of the simulations suggest two routes for aging process acceleration. The first option is to insulate the aging vessel to prevent heat losses. Eliminating heat losses would slightly increase the slope of the heating curve in the outermost sections of blanket and, perhaps more importantly, increase the final temperature in these sections. As discussed in Section 2.1.2, the rate of aging is a strong function of process temperatures, indicating once at temperature the alcogel blanket would age more quickly in an insulated vessel than in an

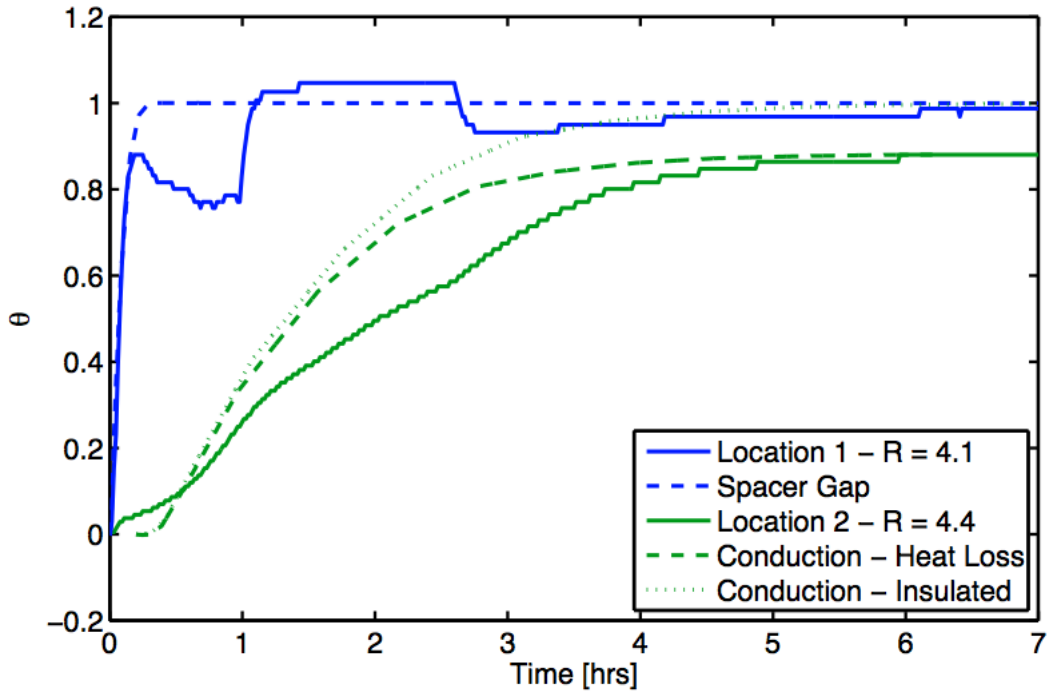

Figure 4.10: Summary of modeling results and aging vessel data

uninsulated one.

The second route for aging process acceleration requires re-evaluating the separator design to keep flow paths between layers unobstructed. In order to decrease the heating times of the outer layers significantly, ethanol must be able to flow between layers and heat them convectively. A comparison of the Conduction Model and the Spacer Gap Model results indicate how significant even a modest flow of ethanol can be in decreasing heating times. In the ideal cases of the models, introducing flow into the outer layers could decrease heating times by almost 3 hours. A redesign of the separator should aim to prevent flow pathways from closing.

CHAPTER V

Conclusions and Future Work

The thermal conductivity of fiber reinforced silica alcogel has been measured using the transient line-source technique and found to be a weak function of aging time. During aging at 60 °C, alcogel thermal conductivity (0.25 W/m·K) decreases by 5-8 % and there is a narrowing of the thermal conductivity distribution. In agreement with the results of the mechanical properties experiments, the decrease in alcogel thermal conductivity ceases after 6 hours of aging. The wide distribution of measured values, significantly greater than the estimated uncertainty of the measurement, has been attributed to variations in the pattern and density of the reinforcing fibers. This wide distribution, combined with the relatively small changes caused by aging, make process monitoring by in-situ property measurement impractical. A better approach would be to monitor the temperature of aging alcogel and use information generated by these experiments to predict aging completion. For example, if a section of blanket has been at 60 °C for 6 hours, the results of these experiments indicate the gel should be sufficiently aged. Future thermophysical property experiments should avoid use of Silbond H5. Better control and repeatability can be achieved by creating TEOS based alcogels through a carefully designed two step acid-based sol-gel process.

The Conduction and Spacer Gap Models were developed to represent heat transfer and fluid flow within the aging vessel. The Conduction Model represents the worst case scenario in the aging vessel, where high stresses block the flow of hot aging fluid, resulting in slow

blanket heating by conduction. The Spacer Gap Model represents the best case scenario, where flow channels are completely unobstructed and the roll heats very quickly. These models provide a good match to temperature data collected from aging vessels. The results of the models demonstrate the importance of keeping channels between layers unobstructed. Redesigning the separator mesh to prevent flow blockages could help decrease blanket heating times, and therefore aging times, by several hours. Additionally, there are significant heat losses in the outer layers of the aging vessel which slow heating times and prevent the gel from reaching operating temperatures. Prevention of these losses would decrease aging times, however, the potential gains are minimal when compared to the gains that a redesign of the separator would provide. For this reason, future work should focus on designing a separator that does not embed into the alcogel blanket under high compressive or winding stresses.

BIBLIOGRAPHY

[1] G. W. Scherer. Aging and drying of gels. *Journal of Non-Crystalline Solids*, 100:77–92, 1988.

[2] S. Smitha, P. Shajesh, S. Rajesh Kumar, P. Krishna Pillai, and K. G. K. Warrier. Effect of aging temperature on the porosity characteristics of subcritically dried silica aerogels. *Microporous and Mesoporous Materials*, 91:286–292, 2006.

[3] P. J. Davis, C. J. Brinker, and D. M. Smith. Pore structure evolution in silica gel during aging/drying I. Temporal and thermal aging. *Journal of Non-Crystalline Solids*, 142:189–196, 1992.

[4] COMSOL AB, Burlington, MA. *COMSOL Multiphysics v4.0 User's Guide*, April 2010.

[5] J. Phalippou, G. W. Scherer, T. Woignier, D. Bourret, and R. Sempéré. Ultraporous materials with low permeability. *Journal of Non-Crystalline Solids*, 186:64–72, 1995.

[6] S. S. Kistler. Coherent expanded aerogels and jellies. *Nature*, 127:741, 1931.

[7] A. Soleimani Dorcheh and M. H. Abbasi. Silica aerogel; synthesis, properties and characterization. *Journal of Materials Processing Technology*, 199:10–16, 2008.

[8] Y. K. Akimov. Fields of application of aerogels (review). *Instruments and Experimental Techniques*, 46(3):287–299, 2003.

[9] M. Schmidt and F. Schwertfeger. Applications for silica aerogel products. *Journal of Non-Crystalline Solids*, 225:364–368, 1998.

[10] T. Woignier, J. Phalippou, J. F. Quinson, M. Pauthe, and F. Laveissiere. Physicochemical transformation of silica gels during hypercritical drying. *Journal of Non-Crystalline Solids*, 145:25–32, 1992.

[11] Aspen Aerogels, Inc. http://www.aerogel.com/, 2010.

[12] M. A. Sherman. Modeling alcogel physical properties during the aging process. Master's thesis, Tufts University, 2010.

[13] Ethyl silicate. Product information, Silbond Corporation, 9901 Sand Creek Highway, P.O. Box 200, Weston, MI 49289, 2010.

[14] C. J. Brinker and G. W. Scherer. *Sol-Gel Science: The physics and chemistry of sol-gel processing*. Academic Press, 1990.

[15] S. Smitha, P. Shajesh, P. R. Aravind, S. Rajesh Kumar, P. Krishna Pillai, and K. G. K. Warrier. Effect of aging time and concentration of aging solution on the porosity characteristics of subcritically dried silica aerogels. *Microporous and Mesoporous Materials*, 91:286–292, 2006.

[16] G. W. Scherer. Mechanics of syneresis I. Theory. *Journal of Non-Crystalline Solids*, 108:18–27, 1989.

[17] G. W. Scherer. Mechanics of syneresis II. Experimental study. *Journal of Non-Crystalline Solids*, 108:28–36, 1989.

[18] S. Hæreid, J. Anderson, M. A. Einarsrud, D. W. Hua, and D. M. Smith. Thermal and temporal aging of TMOS-based aerogel precursors in water. *Journal of Non-Crystalline Solids*, 185:221–226, 1995.

[19] P. J. Davis, C. J. Brinker, D. M. Smith, and R. A. Assink. Pore structure evolution in silica gel during aging/drying II. Effect of pore fluids. *Journal of Non-Crystalline Solids*, 142:197–207, 1992.

[20] S. Hæreid, E. Nilsen, and M. A. Einarsrud. Properties of silica gels aged in teos. *Journal of Non-Crystalline Solids*, 204:228–234, 1996.

[21] J. L. Gurav, A. V. Rao, and D. Y. Nadargi. Study of thermal conductivity and effect of humidity on HMDZ modified TEOS based aerogel dried at ambient pressure. *Journal of Sol-Gel Science and Technology*, 50:275–280, 2009.

[22] P. J. Davis, R. Deshpande, D. M. Smith, C. J. Brinker, and R. A. Assink. Pore structure evolution in silica gel during aging/drying IV. Varying pore fluid ph. *Journal of Non-Crystalline Solids*, 167:295–306, 1994.

[23] S. Hæreid, E. Nilson, V. Ranum, and M. A. Einarsrud. Thermal and temporal aging of two step acid-base catalyzed silica gels in water/ethanol solutions. *Journal of Sol-Gel Science and Technology*, 8:153–157, 1997.

[24] R. Deshpande, D. W. Hua, D. M. Smith, and C. J. Brinker. Pore structure evolution in silica gel during aging/drying III. Effects of surface tension. *Journal of Non-Crystalline Solids*, 144:32–44, 1992.

[25] L. Kocon, F. Despetis, and J. Phalippou. Ultralow density silica aerogels by alcohol supercritical drying. *Journal of Non-Crystalline Solids*, 225:96–100, 1998.

[26] P. H. Tewari, A. J. Hunt, and K. D. Lofftus. Ambient-temperature supercritical drying of transparent silica aerogels. *Materials Letters*, 3(9, 10):363–367, 1985.

[27] Standard test method for steady-state heat flux measurements and thermal transmission properties by means of the guarded-hot-plate apparatus. ASTM Standard C 177-04, ASTM International, Conshohocken, PA, 2004.

[28] Standard test method for steady-state thermal transmission properties by means of the heat flow meter apparatus. ASTM Standard C 518-04, ASTM International, Conshohocken, PA, 2004.

[29] R. Kempers, P. Kolodner, A. Lyons, and A.J. Robinson. Development of a high-accuracy thermal interface material tester. In *Thermal and Thermomechanical Phenomena in Electronic Systems, 2008. ITHERM 2008. 11th Intersociety Conference on*, pages 221–226, May 2008.

[30] Standard test method for thermal conductivity of plastics by means of a transient line-source technique. ASTM Standard D 5930-01, ASTM International, Conshohocken, PA, 2001.

[31] E. Takegoshi, S. Imura, Y. Hirasawa, and T. Takenaka. A method of measuring the thermal conductivity of solid materials by transient hot wire method of comparison. *Bulletin of the JSME*, 25(201):395–402, 1982.

[32] U. B. Holeschovsky, G. T. Martin, and J. W. Tester. A transient spherical source method to determine thermal conductivity of liquids and gels. *International Journal of Heat and Mass Transfer*, 39(6):1135–1140, 1996.

[33] B. Stalhane and S. Pyk. New method for determining the coefficients of thermal conductivity. *Teknisk Tidskrift*, 61:389–393, 1931.

[34] E. F. M. van der Held and F. G. van Drunen. A method of measuring the thermal conductivity of liquids. *Physica*, 15(10):865–881, 1949.

[35] H. Bjurstrm, E. Karawacki, and B. Carlsson. Thermal conductivity of a microporous particulate medium: moist silica gel. *International Journal of Heat and Mass Transfer*, 27(11):2025–2036, 1984.

[36] Y. Y. Tanashev and Y. I. Aristov. Thermal conductivity of a silica gel and calcium chloride system: the effect of adsorbed water. *Journal of Engineering Physics and Thermophysics*, 73(5):876–883, 2000.

[37] M. Shariaty-Niassar, M. Hozawa, and T. Tsukada. Development of probe for thermal conductivity measurement of food materials under heated and pressurized conditions. *Journal of Food Engineering*, 43(3):133–139, 2000.

[38] H. Lobo and C. Cohen. Measurement of thermal conductivity of polymer melts by the line-source method. *Polymer Engineering and Science*, 30(2):65–70, 1990.

[39] S. Q. Zeng, A. J. Hunt, W. Cao, and R. Greif. Pore size distribution and apparent gas thermal conductivity of silica aerogel. *Journal of Heat Transfer*, 116(3):756–759, 1994.

[40] S. Q. Zeng, A. J. Hunt, and R. Greif. Geometric structure and thermal conductivity of porous medium silica aerogel. *Journal of Heat Transfer*, 117(4):1055–1058, 1995.

[41] J. H. Blackwell. A transient-flow method for determination of thermal constants of insulating materials in bulk. *Journal of Applied Physics*, 25(2):137–144, 1954.

[42] G. C. Glatzmaier and W. F. Ramirez. Simultaneous measurement of the thermal conductivity and thermal diffusivity of unconsolidated materials by the transient hot wire method. *Review of Scientific Instruments*, 56(7):1394–1398, 1985.

[43] H. S. Carslaw and J. C. Jaeger. *Conduction of Heat in Solids*. Oxford University Press, second edition, 1959.

[44] E. G. Murakami, V. E. Sweat, S. K. Sastry, and E. Kolbe. Analysis of various design and operating parameters of the thermal conductivity pobe. *Journal of Food Engineering*, 30(1-2):209–225, 1996.

[45] G. Nellis and S. Klein. *Heat Transfer*. Cambridge University Press, first edition, 2009.

[46] D. D. Smith, L. Sibille, E. Ignont, R. J. Cronise, and D. A. Noever. Noble metal immersion spectroscopy of silica alcogels and aerogels. *Journal of Porous Materials*, 7:499–508, 2000.

[47] S. J. Kline and F. A. McClintock. Describing uncertainties in single-sample experiments. *Mechanical Engineering*, pages 3–8, January 1953.

[48] Agilent Technologies. *User's Guide: Agilent Technologies E3633A and E3634A DC Power Supplies*, 2 edition, April 2000.

[49] National Instruments. *NI 9211 4-Channel Thermocouple Input Module Operating Instructions and Specifications*, June 2009.

[50] G. Samsonov. *The Oxide Handbook*, page 122. IFI/Plenum, 1973.

[51] R. C. Reid, J. M. Prausnitz, and B. E. Poling. *The Properties of Gases and Liquids*, page 547. McGraw-Hill, Co., 4 edition, 1987.

[52] G. W. Scherer. Personal interview, December 2010.

[53] I. B. Celik. Procedure for estimation and reporting of uncertainty due to discretization in CFD applications. *Journal of Fluids Engineering*, 130(7):078001, 2008.